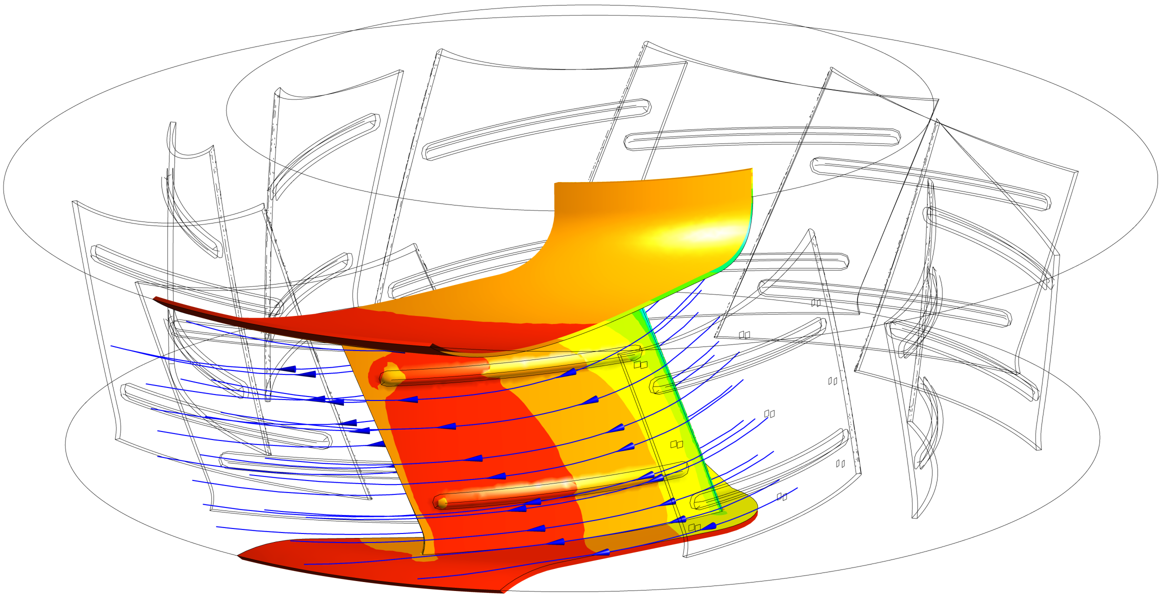

Fluid-Structure Interaction Analysis of a Centrifugal Fan

A Numerical Study to Investigate the Necessity of Including Aerodynamic Loads in Fatigue Estimation

Master's thesis in Applied Mechanics

DAVID KALLIN
KNUT NORDENSKJÖLD

Department of Applied Mechanics
CHALMERS UNIVERSITY OF TECHNOLOGY
Gothenburg, Sweden 2017

Master's thesis in applied mechanics

Fluid-Structure Interaction Analysis of a Centrifugal Fan

A Numerical Study to Investigate the Necessity of Including Aerodynamic Loads in Fatigue Estimation

DAVID KALLIN
KNUT NORDENSKJÖLD

CHALMERS
UNIVERSITY OF TECHNOLOGY

Department of Applied Mechanics
Division of Fluid Mechanics
Chalmers University of Technology
Gothenburg, Sweden 2017

Fluid-Structure Interaction Analysis of a Centrifugal Fan
A Numerical Study to Investigate the Necessity of Including Aerodynamic Loads in Fatigue Estimation
DAVID KALLIN
KNUT NORDENSKJÖLD

Supervisors: Andreas Gustafsson, Federico Ghirelli, Johan Olsson, SEMCON
Examiner: Professor Lars Davidson, Applied Mechanics

Master's Thesis 2017:54
ISSN 1652-8557
Department of Applied Mechanics
Division of Fluid Mechanics
Chalmers University of Technology
SE-412 96 Gothenburg
Sweden
Telephone +46 31 772 1000

Cover: Wire-frame model of the centrifugal fan with pressure contours on the surfaces of one fan sector as well as streamlines around one of the fan blades.

Typeset in LaTeX
Printed by: Department of Applied Mechanics
Gothenburg, Sweden 2017

Fluid-Structure Interaction Analysis of a Centrifugal Fan
A Numerical Study to Investigate the Necessity of Including Aerodynamic Loads in Fatigue Estimation
DAVID KALLIN
KNUT NORDENSKJÖLD
Department of Applied Mechanics
Division of Fluid Mechanics
Chalmers University of Technology

Abstract

Centrifugal fans are used within many applications where great ability to create pressure increase is of importance. Rotating machinery such as industrial fans are often expected to withstand a very large number of load cycles with little or no maintenance. Consequently, accurate estimation of the fatigue limit is of interest when designing a centrifugal fan. It is known that pressure fluctuations arise on the fan leading to time varying loads. It is proposed that these pressure fluctuations have an impact on the fatigue limit of the centrifugal fan studied in this work. This study investigates the capabilities of estimating the fatigue limit based on fluid-structure interaction with commercial software.

In this study, a method of simulating fluid-structure interaction has been applied on a centrifugal fan with the commercial software platform ANSYS Workbench. The method involves simulation of the unsteady turbulent flow through the fan as well as, static and transient, structural analysis. Fluid analysis has been performed on the deformed shape on the fan caused by centrifugal force. Pressure fluctuations on the fan surface are analysed and applied to the fan in a transient structural simulation to obtain the stress variations in critical locations. A crude estimate of the fatigue limit has been done based on the obtained stress field.

Blade pressure fluctuations are captured in simulations and interesting correlations between the blade surface fluctuations and the surrounding flow structures are found. Results shows a weak interaction between structural and fluid field suggesting that a one-way coupled approach is adequate when performing fluid-structure interaction simulations of the studied fan. Aerodynamic loads are found to have a negligible impact on the estimated fatigue life. The main weakness of this work is the lack of verification of the numerical simulations.

Keywords: Fluid-structure interaction (FSI), Centrifugal fan, Finite element analysis (FEA), Computational Fluid Dynamics (CFD), Fatigue.

Preface

This master's thesis was written during the spring of 2017 and completes the master's programme Applied Mechanics at Chalmers University of Technology in Gothenburg, Sweden. The work has been proposed by the Swedish ventilation manufacturer Swegon and carried out at the engineering consultancy company Semcon in Gothenburg.

Acknowledgements

We would like to express our gratitude to Swegon for proposing such an interesting master's thesis, giving us the opportunity to apply advanced engineering tools in the area of ventilation fans. We would like to thank Martin Ottersten at Swegon for always providing needed information and valuable discussions. Many thanks to Federico Ghirelli, Erik Sjösvärd, Andreas Gustafsson and Johan Olsson who showed great knowledge and unremitting support in everything from decision making to technical issues. Big thanks to Daniel Tappert who always showed great support in all administrative matters concerning the project. We also wish to thank everyone else at the simulation department at Semcon for making the time spent there very pleasant. Finally we wish to thank Professor Lars Davidson for taking the effort and responsibility of supervisor and examiner of this thesis.

David Kallin, Knut Nordenskjöld, Gothenburg, June 2017

Nomenclature

Symbols

$\boldsymbol{h}_\Gamma(t)$	Traction vector on fluid-structure interface
$[S_e]$	Element stress stiffening matrix
$\beta^*,\ \beta,\ \alpha,\ \sigma_k,\ \sigma_\omega$	Turbulence model constants
$\boldsymbol{A}$	Vector of total displacements
$\boldsymbol{x}_\Gamma(t)$	Position vector of fluid-structure interface
Δt	Time step
δ_{ij}	Kroneckerdelta tensor
$\dot{E}$	Internal energy rate of change
$\dot{H}$	Rate of added heat
$\dot{M}$	Mass rate of change
$\dot{N}$	Angular momentum rate of change
$\dot{P}$	Momentum rate of change
$\dot{W}$	Rate of work done
ϵ	Turbulent dissipation rate
ϵ_{ijk}	Alternating tensor to describe cross product
ϵ_{ij}	Biot strain tensor
Γ	Domain of integration (Surface)
Γ_d	Diffusion coefficient
κ	Arbitrary variable
λ, μ_l	Lame's constants
$\mathcal{E}$	Net radiative heat source
$\mathcal{L}$	Turbulent length scale
$\mathcal{U}$	Turbulent velocity scale
μ	Dynamic viscosity
μ_f	Coefficient of friction
ν	Kinematic viscosity
ν_p	Poisson's ratio
ν_t	Turbulent viscosity
Ω	Domain of integration (Volume)
ω	Specific rate of dissipation
ω_i	Planar rotation tensor
ω_s	Point mass angular velocity
Ω_{ij}	Vorticity tensor
$\overline{\Omega}$	Absolute vorticity
$\overline{v}$	Velocity parallel to wall
$\overline{v}^*$	Dimensionless flow velocity parallel to wall

$\overline{v}_i$	Averaged velocity tensor
ϕ	Scalar field
ρ	Density
σ_R	Stress range
σ_{10^7}	Stress range at which fatigue limit is 10^7
σ_{ij}	Stress tensor
τ_w	Wall shear stress
τ_{ij}	Viscous stress tensor
C_μ	Turbulence model constant
C_{ijkl}	Hooke's stiffness tensor
D	Outlet/Inlet diameter
E	Empirical constant for log-law
e	Internal energy
E_{ij}	Green-Lagrange strain tensor
E_{mod}	Young's modulus
F_1, F_2	Blending functions
F_f	Friciton force
F_i	Body force tensor (force per unit mass)
f_i	Body force tensor (force per unit volume)
F_N	Contact normal force
F_{ij}	Deformation gradient tensor
h	Element/cell size
h_0	Initial element/cell size
I	Turbulent intensity
K	Spring stiffness
k	Turbulent kinetic energy
l	Calculated turbulent length scale
M	Mach number
M_i	Torque tensor
N	Fatigue limit (Number of cycles)
P	Static pressure
p	Hydrodynamic pressure
P_k	Production of turbulent kinetic energy
q_n	Heat flux
r	Point mass radial rest position
R_e	Reynolds number
r_i	Position tensor
R_{ij}	Rigid rotation tensor
S_ϕ	Source term of ϕ
S_{ij}	Strain-rate tensor
t	Time
t_i	Traction tensor
u	Spring radial displacement
u_i	Displacement tensor
U_{ij}	Shape change tensor
v'_i	Fluctuating velocity tensor

v_i^m	Control volume velocity tensor
v_i	Instantaneous velocity tensor
X_i	Material coordinate tensor
x_i	Spatial coordinate tensor
x_p	Penetration gap
y	Wall normal distance
y^*	Dimensionless wall distance

Abbreviations

CFD	Computational fluid dynamics
FE	Finite element
FEA	Finite element analysis
FEM	Finite element method
FSI	Fluid-strucutre interaction
MPC	Multi-point constraint
SST	Shear stress transport

Contents

List of Figures

List of Tables

1
Introduction

When designing rotating machinery it is important to consider vibrations of the structure as they can cause failure by dynamic instability or fatigue. Fatigue is an area under development in the field of rotating machinery as the components often are expected to withstand a very large number of load cycles. It is not uncommon that rotating machines are subject to fluid flow, such as turbines and fans. As flow passes through rotating machinery, pressure fluctuations arise which can act as a fluctuating load on a fan for example. The cumulative load cycles from such fluctuations might grow very fast. Therefore it is proposed that these fluctuations might have an impact on the life length of a centrifugal fan which is studied in this work. Investing the flow induced vibrations (FIV) falls in the field of fluid-structure interaction (FSI). A method to simulate FSI is adopted to estimate the fluctuating stress in the fan caused by fluid flow.

1.1 Background

Swegon is a company which specialises in indoor climate systems. Key components in the air-handling units are the fans, which have high requirements on performance and durability. Increasing efforts are put into simulating the characteristics of different design solutions in order to achieve better understanding of the product and eventually make educated design improvements.

When designing a sustainable product, estimating the life length or fatigue limit is of great interest. It is known that pressure fluctuations arise on the fan blade from the fact that the flow is turbulent and from earlier studies [1, 2], which raise the question of weather the fluctuations are of any importance when estimating the fatigue limit. Swegon wishes to be able to predict stress fluctuations caused by aerodynamics loads with numerical simulations. Since welds are prone to fatigue, stress fluctuations near welds in the structure are of special interest.

To predict the effect of aerodynamic loads on the stress-field in the fan, FSI simulation is required. Swegon is also generally interested in a method for performing FSI simulation on their fans which is applicable in the industry. FSI is considered a useful tool to be implemented in the product development process but the plausibility in terms of resources and efficiency of the method has not been investigated.

1.2 Purpose & Objectives

The main purpose of this thesis is to make an initial assessment of whether the loads caused by aerodynamic fluctuations are of any significance when testing or estimating the fatigue limit in the welds of the fan. The project can be split in to different objectives:

- Perform numerical simulation of the unsteady flow around the fan that captures pressure fluctuations and investigate the reliability of the result to the best ability with limited verification methods.
- Develop a method for numerical simulation of FSI for the studied fan which is applicable in the industry.
- Perform numerical simulation to estimate the impact of the aerodynamic forces on the stress field in the fan.
- Asses whether aerodynamic loads are of significance when estimating the fatigue limit of the critical welds in the fan.

1.3 Scope

This study considers one fan geometry and one set of operating conditions. The chosen operating conditions are typical for the selected centrifugal fan while in duty. The fluid and structural analyses are performed separate. FSI will be simulated by passing data from one completed analysis (fluid or structure) to another i.e analyses are run sequentially and never at the same time. The work can therefore be divided into a structural analysis part and a fluid analyis part. The stress field in the fan after being subject to aerodynamic loads is calculated but no extensive efforts are put in to achieve an accurate life estimation. The analyses will be performed using the software platform ANSYS Workbench. The Structural analysis will be performed using ANSYS Mechanical and the Fluid analysis using ANSYS Fluent. No experiment will be carried out in this project but data from earlier tests performed at Swegon will be used to verify the results of the CFD simulations. The computational resources are limited and the models and method for performing FSI are designed accordingly.

2

Theory

In the following chapter some theory behind the work is presented to help the reader better understand the concepts and application of different techniques. The chapter contains explanation of fundamental equations describing the physics behind the simulations, some specific aspects of the structural and fluid simulations and brief description of fluid-structure interaction and flow induced vibration.

2.1 Governing Equations

The fundamental equations describing the motion of fluid and solid are stated here as well as the principles they are based on. These equations are the heart of the theory behind fluid and solid mechanics. Different numerical techniques are then used to solve these equations for fluid and solid domains respectively.

2.1.1 Conservation Equations

The principle of conservation of mass states that the total mass within some domain Ω remains constant [3]:

$$\dot{M} = \frac{d}{dt}\int_{\Omega} \rho d\boldsymbol{x} = \int_{\Omega} (\frac{d\rho}{dt} + \rho\frac{\partial v_i}{\partial x_i}) d\boldsymbol{x} = 0 \tag{2.1}$$

The equation holds for all domains Ω and can therefor be written as:

$$\frac{d\rho}{dt} + \rho\frac{\partial v_i}{\partial x_i} = 0 \qquad \text{(Continuity equation)} \tag{2.2}$$

The conservation of linear momentum states that the rate of change of linear momentum $\boldsymbol{P}$ of a domain Ω is governed by the applied force [3]:

$$\dot{P}_i = F_i = \int_{\Omega} \rho\frac{dv_i}{dt} = \int_{\Omega} \rho f_i d\boldsymbol{x} + \oint_{\Gamma} t_i ds = \int_{\Omega} \rho f_i + \frac{\partial \sigma_{ij}}{\partial x_j} d\boldsymbol{x} \tag{2.3}$$

As for conservation of mass the equation holds for all possible domains and can therefore be written as:

$$\frac{\partial \sigma_{ij}}{\partial x_j} + \rho f_i = \rho\frac{dv_i}{dt} \qquad \text{(Momentum equation)} \tag{2.4}$$

The conservation of angular momentum states that the rate of change of angular momentum $\boldsymbol{N}$ of a domain is governed by the applied torque [3]:

$$\dot{N}_i = M_i \tag{2.5}$$

which after some manipulation results in the conclusion that the stress tensor (σ_{ij}) is symmetric.

Conservation of energy states that the rate of change of the internal energy in a domain is determined by the heat added to the system and the work done by the system [3]:

$$\dot{E} = \dot{H} + \dot{W} = \int_\Omega \rho v_i \frac{dv_i}{dt} + \int_\Omega \rho \frac{de}{dt} = \int_\Omega \rho f_i v_i d\boldsymbol{x} + \oint_\Gamma t_i v_i ds + \int_\Omega \rho \mathcal{E} d\boldsymbol{x} + \oint_\Gamma -q_n ds \tag{2.6}$$

Rewriting the expression and using the balance of linear momentum we obtain the energy equation:

$$\rho \frac{de}{dt} - \sigma_{ji} \frac{\partial v_i}{\partial x_j} + \frac{\partial q_i}{\partial x_i} = \rho \mathcal{E} \qquad \text{(Energy equation)} \tag{2.7}$$

2.1.2 Governing Solid Equations

There are typically three equations governing a solid: Equation of motion, strain-displacement relation and a constitutive relation between stress and strain. These will be further explained in this section.

The equation of motion is the same as the momentum equation in Equation 2.4, but here the body force is written directly as a force per unit mass and the acceleration term is written using the displacement u_i instead of velocity. It reads:

$$\frac{\partial \sigma_{ji}}{\partial x_j} + F_i = \rho \frac{\partial^2 u_i}{\partial t^2} \tag{2.8}$$

The strain-displacement relation can be defined in various ways depending on whether large deformation theory should be included and which strain measure is used. Here, large deformation theory and the Biot strain measure is presented. We start by defining displacement vector as:

$$u_i = x_i - X_i \tag{2.9}$$

where x_i and X_i are the position vectors of a point in the deformed and undeformed configuration respectively. Which can also be referred to as *spatial* and *material* coordinate respectively. The deformation gradient is then defined as:

$$F_{ij} = \frac{\partial x_i}{\partial X_j} \tag{2.10}$$

which can be rewritten using Equation 2.9 as:

$$F_{ij} = \delta_{ij} + \frac{\partial u_i}{\partial X_j} \tag{2.11}$$

The deformation gradient can be separated into a rotation and a shape change tensor using the right polar decomposition theorem [4]. The deformation gradient is then expressed as:

$$F_{ij} = R_{ik}U_{kj} \tag{2.12}$$

where R_{ij} is the rotation tensor and U_{ij} is the shape change tensor. Once U_{ij} is known the Biot strain measure is defined as:

$$\epsilon_{ij} = U_{ij} - \delta_{ij} \tag{2.13}$$

This strain measure allows for small strains but large rigid body rotations. Finally the set of differential equations are completed by a set of constitutive equations. Here we consider Hooke's law which reads:

$$\sigma_{ij} = C_{ijkl}\epsilon_{kl} \tag{2.14}$$

Assuming an isotropic homogeneous material the relation can be simplified to:

$$\sigma_{ij} = \lambda\epsilon_{kk}\delta_{ij} + 2\mu_l\epsilon_{ij} \tag{2.15}$$

where λ and μ_l are Lame's constants which ca be written in terms of Young's modulus E_{mod} and Poisson's ratio ν_p as

$$\lambda = \frac{E_{mod}\nu_p}{(1+\nu_p)(1-2\nu_p)} \tag{2.16}$$

$$\mu_l = \frac{E_{mod}}{2(1+\nu_p)} \tag{2.17}$$

These linear algebraic constitutive equations complete the set of differential equations governing the solid.

2.1.3 Governing Flow Equations

The constitutive law for Newtonian viscous fluids is formulated as:

$$\sigma_{ij} = -P\delta_{ij} + 2\mu S_{ij} - \frac{2}{3}\mu S_{kk}\delta_{ij} \tag{2.18}$$

$$\tau_{ij} = 2\mu S_{ij} - \frac{2}{3}\mu S_{kk}\delta_{ij} \tag{2.19}$$

$$S_{ij} = \frac{1}{2}\Big(\frac{\partial v_i}{\partial x_j} + \frac{\partial v_j}{\partial x_i}\Big) \tag{2.20}$$

where τ_{ij} is the viscous stress tensor and S_{ij} is the strain rate tensor [5]. Inserting the constitutive law into Equation 2.4 the Navier-Stokes equations are obtained. The simplified version applicable for constant viscosity and density can be expressed as:

$$\rho\frac{dv_i}{dt} = -\frac{\partial P}{\partial x_i} + \mu\frac{\partial^2 v_i}{\partial x_j \partial x_j} + \rho f_i \tag{2.21}$$

where the body force term ρf_i is often omitted in the case of incompressible flow. For the equation still to hold, the static pressure P has to be exchanged by the hydrodynamic pressure p. When solving Equation 2.21 numerically using finite volume methods, the left hand side of the equation is rewritten into conservative form:

$$\frac{\partial \rho v_i}{\partial t} + \frac{\partial \rho v_j v_i}{\partial x_j} = -\frac{\partial p}{\partial x_i} + \mu \frac{\partial^2 v_i}{\partial x_j \partial x_j} \tag{2.22}$$

For constant density flows the continuity equation 2.2 can be written as:

$$\frac{\partial v_i}{\partial x_i} = 0 \tag{2.23}$$

In the three dimensional case, Equation 2.22 and Equation 2.23 constitutes a system of four equations with four unknowns. The energy equation is not needed unless the problem includes heat transfer or when the flow is compressible and the above made simplification of constant density can not be made.

2.2 Computational Solid Mechanics

To solve the governing differential equations for the solid, i.e the aluminium fan, the finite element method (FEM) is adopted. FEM is widely used in engineering and science to solve partial differential equations and in particular solid mechanics problems. There are numerous aspect of FEM that can be covered in a theory chapter but only a very small part is included here. The topics covered are just beyond the very basics of structural analysis using FEM. The topics treated are geometric nonlinearities in section 2.3 and contact modelling in section 2.4.

2.3 Geometric Nonlinearities

Nonlinearities arise when the deformations are allowed to be arbitrarily large. In finite element analysis (FEA) this is often called accounting for large deflections. These effects are referred to as geometric nonlinearities. Two properties of geometric nonlinearity which are relevant to this study are discussed in this section, spin softening and stress stiffening.

2.3.1 Spin Softening

Consider a point mass attached to a spring rotating around an axis perpendicular to the spring as shown in Figure 2.1. Equilibrium for the system assuming small deflection reads:

$$Ku = \omega_s^2 m r \tag{2.24}$$

where u is the radial displacement from the rest position, r is the radial rest position and ω_s is the angular velocity. Accounting for large deflections Equation 2.24 becomes:

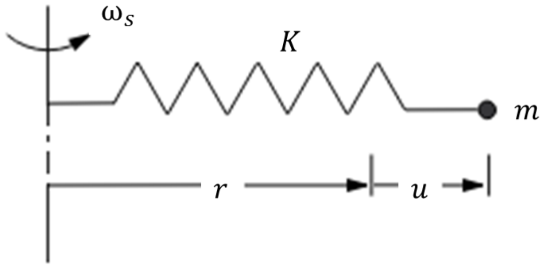

Figure 2.1: Rotating point mass attached to spring

$$Ku = \omega_s^2 m(r+u) \Leftrightarrow (K - \omega_s^2 M)u = \omega_s^2 mr \tag{2.25}$$

which results in the new reduced stiffness $\overline{K} = (K - \omega_s^2 m)$. This softening effect is referred to as spin softening [4]. This is an example of accounting for large deflection in a small deflection solution (linear equation). In a large deflection analysis in ANSYS this effect is automatically accounted for and no special spin softening contribution is made to the stiffness matrix. In summary, the loads dependence on the deflection is accounted for which results in a greater load (or softer structure).

2.3.2 Stress Stiffening

Stress stiffening is the transverse stiffening of a slender structure which is loaded in axial direction producing membrane stresses in the structure as illustrated in Figure 2.2. Stress stiffening is accounted for by calculating an additional stiffness matrix which is added to the normal stiffness. The stiffness contribution is based on the Green-Lagrange strain defined as:

$$E_{ij} = \frac{1}{2}\Big(\frac{\partial u_i}{X_j} + \frac{\partial u_j}{X_i} + \frac{\partial u_k}{X_i}\frac{\partial u_k}{X_j}\Big) \tag{2.26}$$

Here, distinction is made between *Spatial* (x_i) and *Material* (X_i) coordinates defined as in Equation 2.9. The element stiffness contribution for stress-stiffening is written symbolically (As it differs depending on element type, see [4]) as:

$$[S_e] = \int_{vol} [G_e]^T [\tau_e][G_e] d(vol) \tag{2.27}$$

where $[G_e]$ is a matrix containing shape function derivatives and $[\tau_e]$ is a matrix containing stresses calculated based on the Green-Lagrange strain.

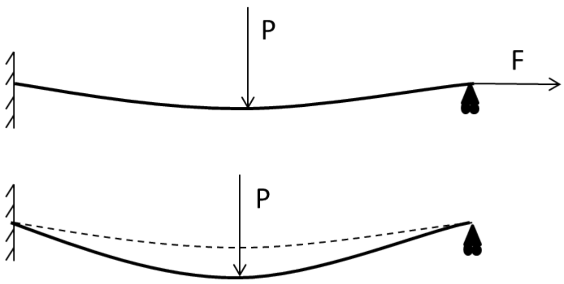

Figure 2.2: Two slender beams deflect differently depending on the axial loading

2.4 Contact Modelling

Contacts between different parts of the fan are modelled in the structural analyses. Contacts can be formulated differently depending on the desired contact behaviour. Two types of formulations are briefly described here, namely Penalty method and Multi-point constraint (MPC).

- The principle of the penalty method is illustrated in Figure 2.3. Forces proportional to the penetration gap x_p are put on the nodes in contact. This can be thought of as putting stiff springs in the gap as shown in Figure 2.3. For the gap to close completely the spring stiffness needs to approach infinity which is numerically impossible. This leads to a small gap when using the penalty method but it is sufficiently accurate in many applications. The gap does not have to be defined by normal penetration of the bodies but can also be defined by separation and sliding between bodies. The penalty method is described in detail in [6].

- Multi-point constraint contact formulation imposes constraint equations on the nodes in contact, which are predefined. The nodes are then constrained in their relative motion. In the case of bonded contact, where no sliding, separation or penetration is allowed, the nodes are rigidly connected. This method is direct and exhibits good convergence behaviour.

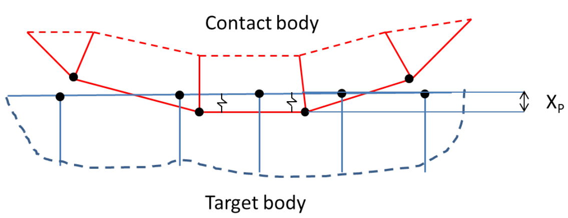

Figure 2.3: Two FE meshes coming into contact creating a small penetration gap x_p. Springs illustrate the force applied in order to close the gap

2.5 Computational Fluid Dynamics

To solve the governing differential equations for the fluid domain, i.e the air surrounding the fan, the finite volume method is adopted. Covered here are some of the fundamentals as well as some specific topics related to simulations which includes rotating components. The governing flow equations solved in the project are time averaged which is described in section 2.5.1. The time averaging results in additional terms that needs to be modelled referred to as turbulence modelling, which is together with the model used in this project, the $k-\omega$ SST turbulence model, outlined in section 2.5.2. Employing the finite volume method, the continuous differential flow equations are translated to discrete algebraic equations, explained in section 2.5.3. The influence of solid walls on the flow and special treatments employed in ANSYS Fluent is described in section 2.5.4. Techniques used for simulating the fan rotation in steady state as well as transient simulations is outlined in section 2.5.5 and 2.5.6 respectively.

2.5.1 Averaging

The flow associated with the fan is turbulent. An exact definition of turbulent flow is yet to be established, for characteristic features of turbulence see for instance [7]. The phenomena is associated with an irregular and chaotic flown field in which the range of spatial and temporal scales are large. Resolving the whole range of scales require large amount of computational resources. A well established procedure to circumvent this is to apply Reynolds decomposition in which the flow field is divided into an averaged and a fluctuating part. Decomposition of an arbitrary variable κ reads:

$$\kappa = \overline{\kappa} + \kappa' \tag{2.28}$$

where the time averaged value is denoted by the bar and calculated as:

$$\overline{\kappa} = \frac{1}{2T}\int_{-T}^{T} \kappa dt \tag{2.29}$$

Decomposing velocity as well as pressure and inserting them into Equation 2.22 and Equation 2.23 yields the time averaged Navier-Stokes equations or the Reynolds-averaged Navier–Stokes equations and the time averaged continuity equation:

$$\rho\frac{\partial \overline{v}_i}{\partial t} + \rho\frac{\partial \overline{v}_i\overline{v}_j}{\partial x_j} = -\frac{\partial \overline{p}}{\partial x_i} + \frac{\partial}{\partial x_j}\left(\mu\frac{\partial \overline{v}_i}{\partial x_j} - \rho\overline{v_i'v_j'}\right) \tag{2.30}$$

$$\frac{\partial \overline{v}_i}{\partial x_i} = 0 \tag{2.31}$$

The new term $\rho\overline{v_i'v_j'}$ appears in Equation 2.30. It is often referred to as the Reynolds stress tensor. It is a new stress term, in addition to the viscous stress, which represents the turbulent contribution to the total stress tensor and it originates from correlations between fluctuating velocities [8]. Since the number of equations are the same as before the new term needs to be modelled, referred to as turbulence modelling.

2.5.2 Turbulence Modelling

When solving the time averaged Naiver-Stokes equations 2.30 and the time average continuity equation 2.31, models used for estimating the turbulent stresses are needed. The most complete models are the Reynolds stress models, where transport equations for all components of the Reynolds stress tensor are solved for. A group of less computationally demanding models are the eddy viscosity models in which a turbulent viscosity used to model all of the Reynolds stresses is introduced. The stresses are modelled using Boussinesq assumption which reads:

$$\overline{v_i'v_j'} = -\nu_t\left(\frac{\partial \overline{v}_i}{\partial x_j} + \frac{\partial \overline{v}_j}{\partial x_i}\right) + \frac{1}{3}\delta_{ij}\overline{v_k'v_k'} = -2\nu_t\overline{s}_{ij} + \frac{2}{3}\delta_{ij}k \tag{2.32}$$

where ν_t is the turbulent viscosity [8]. It is estimated as a product of a turbulent velocity and a turbulent length scale [8]:

$$\nu_t \propto \mathcal{U}\mathcal{L} \tag{2.33}$$

Well studied models are the $k-\epsilon$ and the $k-\omega$ model. These are two equation models that solve transport equations for two turbulent quantities. The $k-\epsilon$ model solves transport equations for the turbulent kinetic energy k as well as the turbulent dissipation rate ϵ. The $k-\omega$ model solves for specific dissipation rate ω instead of ϵ. The turbulent viscosity is for the two models obtained as:

$$\nu_t = C_\mu \frac{k^2}{\epsilon} \propto \mathcal{U}\mathcal{L} \qquad (k-\epsilon \text{ model}) \tag{2.34}$$

$$\nu_t = \frac{k}{\omega} \propto \mathcal{U}\mathcal{L} \qquad (k-\omega \text{ model}) \tag{2.35}$$

The $k-\epsilon$ model was introduced by Launder and Spalding, for details regarding the model see [9]. For information about the $k-\omega$ model the reader is instead referred to [10].

2.5.2.1 The Shear Stress Transport Model

The SST model was initially developed for aeronautic applications with focus on being able to accurately predict flows containing adverse pressure gradients [11]. The approach is to combine two existing models, the $k-\omega$ and the $k-\epsilon$ model as well as introducing a limit on turbulent shear stress in adverse pressure gradient regions [11]. Both turbulence models work well in different regions of the flow and by combining them a model with the potential of more accurately predicting the flow characteristics of the whole domain is obtained. The main drawback of the $k-\omega$ model is its sensitivity to the free stream values of ω [12]. For the $k-\epsilon$ model, the drawback is a need for near wall modification together with overprediction of turbulent shear stress in flows containing adverse pressure gradients. The $k-\omega$ model on the other hand does not need any near wall modifications and have been shown to more accurately predict regions of adverse pressure gradients [8]. From the above stated drawbacks of respective model it is proposed that a blend of the two models is implemented depending on flow region. The $k-\omega$ model should be implemented in the inner boundary layer while the $k-\epsilon$ model should be implemented outside of the boundary layer and a blend of the two between the extremes. Using the relation $\omega = \epsilon/(\beta^* k)$, the $k-\epsilon$ model is transformed to a model for $k-\omega$. The transformed version of the $k-\epsilon$ model is together with a blending function used to obtain the correct blend between the two models. The SST model is formulated as in [11] and reads:

$$\frac{\partial(\rho k)}{\partial t} + \frac{\partial(\rho \overline{v}_i k)}{\partial x_i} = P_k - \beta^* \rho k \omega + \frac{\partial}{\partial x_i}\left[(\mu + \sigma_k \mu_t)\frac{\partial k}{\partial x_i}\right] \tag{2.36}$$

$$\frac{\partial(\rho \omega)}{\partial t} + \frac{\partial(\rho \overline{v}_i \omega)}{\partial x_i} = \alpha \rho |\overline{s}|^2 - \beta \rho \omega^2 + \frac{\partial}{\partial x_i}\left[(\mu + \sigma_\omega \mu_t)\frac{\partial \omega}{\partial x_i}\right] + 2(1-F_1)\rho \sigma_{w2}\frac{1}{\omega}\frac{\partial k}{\partial x_i}\frac{\partial \omega}{\partial x_i}.$$

where F_1 is the blending function, P_k is the production term, $|\overline{s}|$ is the magnitude of the strain rate and β^*, β, α, σ_k and σ_ω are model constants. The blending function F_1 determines the transition from the $k-\omega$ to the $k-\epsilon$ model. in the near wall region $F_1 = 1$ resulting in the formulation of the $k-\omega$ model. F_1 gradually decrease as the distance to the wall increases and as $F_1 = 0$ the $k-\epsilon$ model is obtained. F_1 is defined as:

$$F_1 = tanh\left[\left[min[max(\frac{\sqrt{k}}{\beta^* \omega y}, \frac{500\nu}{y^2 \omega}), \frac{4\rho \sigma_{\omega 2} k}{CD_{k\omega} y^2}]\right]^4\right] \tag{2.37}$$

where y is the distance to the closest wall and $CD_{k\omega} = max\Big(2\rho\sigma_{\omega 2}\frac{1}{\omega}\frac{\partial k}{\partial x_i}\frac{\partial \omega}{\partial x_i}, 10^{-10}\Big)$.

It is mentioned above that the $k-\omega$ model is more accurate for predicting flows in regions containing adverse pressure gradients compared to the $k-\epsilon$ model. The reason is that the $k-\epsilon$ model over predicts the turbulent shear stress in these regions. Although implementation of the $k-\omega$ model results in a more accurate prediction it has been shown to still over predict the turbulent shear stress. With the aim of reducing this error a limit on turbulent shear stress is introduced using the Johnson-King model. The model is based on a transport equation of the main turbulent shear stress and makes use of Brandshaw's assumption, unlike Boussinesq assumption which is used in both the $k-\omega$ and the $k-\epsilon$ model. In boundary layer flows Brandshaw's assumption and Boussinesq assumption can respectively be written as:

$$-\overline{v_1' v_2'} = a_1 k = \sqrt{\beta^*} k = \sqrt{c_\mu} k \qquad \text{(Brandshaw)} \tag{2.38}$$

$$-\overline{v_1' v_2'} = \nu_t \frac{\partial \overline{v}_1}{\partial x_2} = \sqrt{c_\mu} k \sqrt{\frac{P_k}{\epsilon}} \qquad \text{(Boussinesq)} \tag{2.39}$$

where the turbulent viscosity is expressed $\nu_t = k/\omega$ in the $k-\omega$ model and $\nu_t = (c_\mu k^2)/\epsilon$ in the $k-\epsilon$ model [8]. In boundary layers of adverse pressure gradient flows it have been shown through experiments that $-\overline{v_1' v_2'} \approx \sqrt{c_\mu} k$, and that the production of turbulent kinetik energy P_k is much lager than the dissipation ϵ. With the results stated above in mind, examining Equation 2.39, it can be noted that $-\overline{v_1' v_2'} >> \sqrt{c_\mu} k$ and hence that the Boussinesq assumption over estimates the turbulent shear stress. With the goal to reduce the estimation of the turbulent shear stress in Equation 2.39, one additional expression of the turbulent viscosity is formulated using Johnson-King [8]:

$$\nu_t = -\frac{\overline{v_1' v_2'}}{\overline{\Omega}} = \frac{\sqrt{c_\mu} k}{\overline{\Omega}} \qquad \text{Johnson-King} \tag{2.40}$$

This new expression should only be used in the boundary layers of adverse pressure gradient flows. To accomplish this, the Johnson-King expression for the turbulent viscosity is used together with the regular expression for the turbulent viscosity from the $k-\omega$ model, and a function F_2 ranging from one to zero depending on the local flow properties. ν_t and F_2 are formulated as in [11]:

$$\nu_t = \frac{\sqrt{c_\mu} k}{\max(\sqrt{c_\mu}\omega, F_2 \bar{\Omega})} \tag{2.41}$$

$$F_2 = \tanh\Big[\big[\max\big(\frac{2\sqrt{k}}{\beta^* \omega y}, \frac{500\nu}{y^2 \omega}\big)\big]^2\Big]. \tag{2.42}$$

The standard model has been further developed with two modifications; a limiter is introduced on the production term in Equation 2.36 and the absolute vorticity $\overline{\Omega}$ in Equation 2.41 is exchanged by $|\overline{s}|$. Both modifications seek to improve the model in stagnation regions. The production limiter by reducing the production of turbulence in stagnation regions and $|\overline{s}|$ by limiting ν_t in stagnation regions. The new production term and the strain rate is defined as:

$$P_k = min(P_{k,old}, 10\epsilon) \qquad P_{k,old} = \mu_t \big(\frac{\partial \overline{v}_i}{\partial x_j} + \frac{\partial \overline{v}_j}{\partial x_i}\big)\frac{\partial \overline{v}_i}{\partial x_j} \tag{2.43}$$

$$|\overline{s}| = \sqrt{\big(\frac{\partial \overline{v}_i}{\partial x_j} + \frac{\partial \overline{v}_j}{\partial x_i}\big)\frac{\partial \overline{v}_i}{\partial x_j}} = \sqrt{2\overline{s}_{ij}\overline{s}_{ij}} \tag{2.44}$$

All model constants are calculated as a mix of corresponding constants from the $k-\omega$ and the $k-\epsilon$ model using the blending function F_1 as:

$$\alpha = \alpha_1 F_1 + \alpha_2(1 - F_1) \tag{2.45}$$

where α represents an arbitrary model constant. The model constants and their default values in fluent [13]:

$$\beta^* = 0,09 \quad \beta_1 = 0,075 \quad \beta_2 = 0,0828 \quad \alpha_1 = 0,52 \quad \alpha_2 = 0,31$$

$$\sigma_{k1} = 1,176 \quad \sigma_{k2} = 1,0 \quad \sigma_{\omega 1} = 2,0 \quad \sigma_{\omega 2} = 1,168$$

2.5.3 Discretisation

The continuous differential equations governing the fluid are, when applying the finite volume method, translated into discrete algebraic equations. This is done by integrating the equations over control volumes. All flow equations can be written on the form of a general transport equation integrated over an arbitrary control volume. The integral form of the general transport equation for a scalar ϕ, on an arbitrary control volume Ω is defined as in [13]:

$$\underbrace{\frac{d}{dt}\int_{\Omega}\rho\phi dV}_{\text{Transient term}}+\underbrace{\int_{\delta\Omega}\rho\phi(v_i-v_i^m)n_i dA}_{\text{Convection term}}=\underbrace{\int_{\delta\Omega}\Gamma_d\frac{\partial\phi}{\partial x_i}n_i dA}_{\text{Diffusion term}}+\underbrace{\int_{\Omega}S_\phi dV}_{\text{Source term}} \tag{2.46}$$

where Γ_d is the diffusion coefficient, S_ϕ is the source term of ϕ and v_i^m is the control volume's velocity tensor. As an example, the Navier-Stokes equations can be obtained by letting $\phi = v_j$, $\Gamma_d = \nu$ and $S_\phi = \partial p/\partial x_j$. The transient term in Equation 2.46 can be simplified in the case of a non-deforming control volume [14]:

$$\underbrace{\int_{\Omega}\frac{\partial}{\partial t}(\rho\phi)dV}_{\text{Transient term}}+\int_{\delta\Omega}\rho\phi(v_i-v_i^m)n_i dA=\int_{\delta\Omega}\Gamma_d\frac{\partial\phi}{\partial x_i}n_i dA+\int_{\Omega}S_\phi dV \tag{2.47}$$

In the case of a fixed non-deforming control volume, both the transient and convection term can be simplified [14]:

$$\underbrace{\int_{\Omega}\frac{\partial}{\partial t}(\rho\phi)dV}_{\text{Transient term}}+\underbrace{\int_{\delta\Omega}\rho\phi v_i n_i dA}_{\text{Convection term}}=\int_{\delta\Omega}\Gamma_d\frac{\partial\phi}{\partial x_i}n_i dA+\int_{\Omega}S_\phi dV \tag{2.48}$$

The flow equations are integrated over the whole domain that have been divided into a number of control volumes. Dependent on the control volumes, the transport equations on one of the forms above are implemented.

2.5.4 Turbulent Boundary Layers

Adjacent to solid surfaces, turbulent fluid flow forms turbulent boundary layers. These are often divided into different regions which are characterises by the forces dominating in respective region.

Roughly 10-20% of the boundary layer is labelled as the inner region. The shear stress is almost constant is this region and equal to the wall shear stress. The inner region is further divided into: the viscous sub-layer, the buffer layer and the log-law layer. The viscous sub-layer is positioned closest to the wall and is, in comparison to other layers, very thin. Turbulence is limited and the motion is dominated by viscous effects. As the distance to the wall increases, the turbulent stresses increases as well. The layer in which viscous and turbulent stresses are of similar magnitude is labelled as the buffer-layer. The log-law layer is situated as the distance to the wall increase further to such an extent that the turbulent stresses dominates the fluid motion. The remaining 80-90 % is labelled as the outer region. The motion is inertia dominated and practically free from viscous effects [15].

The flow quantities experience large wall normal gradients in the inner region. The computational mesh therefor needs to be of high resolution in the wall normal direction if the boundary layer should be fully resolved by integration of the governing equations all the way to the wall. To reduce the mesh size and thereby reduce the computational resources needed, wall functions are commonly applied. Wall functions estimates the fluid quantities in the wall adjacent cells by empirically correlated functions which, in ANSYS Fluent, uses the dimensionless wall normal distance y^* to approximate where in the boundary layer the first cell node is located. y^* is defined as:

$$y^* = \frac{\rho C_\mu^{1/4} k y}{\mu} \tag{2.49}$$

where C_μ is a model constant, k is the turbulent kinetic energy and y is the wall normal distance [13]. Note that y^* is approximately equal to the more often used dimensionless wall normal distance y^+ in equilibrium turbulent boundary layers [13].

Wall functions are for the case of velocity formulated with the law of the wall which states that the mean velocity in the viscous sub-layer and log-law layer can be obtained respectively as [13]:

$$\overline{v}^* = y^* \qquad \text{(viscous sub-layer)} \tag{2.50}$$

$$\overline{v}^* = \frac{1}{\kappa} ln(E y^*) \qquad \text{(log-law layer)} \tag{2.51}$$

where

$$\overline{v}^* = \frac{\overline{v} C_\mu^{1/4} k^{1/2}}{\tau_w / \rho} \tag{2.52}$$

in which $\overline{v}$ is the flow velocity parallel to the wall, E is an empirical constant and τ_w is the wall shear stress.

2.5.5 Rotating Reference Frame

Many problems which involves rotating components can be modelled using a rotating reference frame. A flow field which is unsteady with respect to the inertial (stationary) frame becomes steady with respect to the rotating frame and hence much easier to solve. Equations of fluid dynamics defined with respect to the moving frame have additional acceleration terms which affect the fluid motion in the moving frame. Modelling motion with a moving reference frame to enable steady state solution is often referred to as the *Frozen Rotor Approach*. The relation between a rotating reference frame (R) and an inertial reference frame (I) for the time derivative of a general tensor A_i is written as:

$$\left[\frac{dA_i}{dt}\right]_I = \left[\frac{dA_i}{dt}\right]_R + \epsilon_{ijk}\omega_j A_k \tag{2.53}$$

Applying this relation to the position tensor r_i, a relation for the velocities (v_i) in each frame is obtained as:

$$\left[\frac{dr_i}{dt}\right]_I = \left[\frac{dr_i}{dt}\right]_R + \epsilon_{ijk}\omega_j r_i \tag{2.54}$$

$$[v_i]_I = [v_i]_R + \epsilon_{ijk}\omega_j r_i \tag{2.55}$$

where ϵ_{ijk} is the alternating tensor to describe cross product in tensor notation and ω_i describes the planar rotation of the frame. The In-compressible Navier-stokes equation and continuity equation are written in the inertial frame of reference with the absolute velocity as in Equations 2.22 & 2.23 respectively. Using the relation between inertial and relative velocities in Equation 2.54 and applying it in Equations 2.22 & 2.23, the Navier-stokes and continuity equation are written in the rotating frame with the absolute velocity as:

$$\frac{\partial [v_i]_R}{\partial t} + \epsilon_{ijk}\frac{d\omega_j}{dt}r_k + \frac{\partial [v_j]_R [u_i]_I}{\partial x_j} + \epsilon_{ijk}\omega_j [v_k]_I = -\frac{\partial p}{\rho \partial x_i} + \nu \frac{\partial^2 [v_i]_I}{\partial x_j \partial x_j} \tag{2.56}$$

$$\frac{\partial [v_i]_I}{\partial x_i} = 0 \tag{2.57}$$

Equations 2.56 & 2.57 are solved in the moving reference frame which enables steady state solutions of problems with moving components. A technique widely used in rotating machinery design. A full derivation of Equations 2.56 & 2.57 can be found at [16].

2.5.6 Sliding Mesh

Employing the sliding mesh method in ANSYS Fluent, the domain is divided into stationary and moving zones. The method allows for the moving zones to translate and/or rotate as a function of time but not to deform. Different zones can be meshed independently from each other and connected via non-conformal mesh-interfaces on which the variables are interpolated between the zones. Since deformation of the zones are prohibited, all mesh cells keeps a constant size and transport equations on the form of Equation 2.48 are used for discretisation in the stationary zones and on the form of Equation 2.47 in the moving zones. The sliding mesh method is only applicable for transient simulations as the solution is inherently unsteady for meshes that move [13].

2.6 Fluid-Structure Interaction

Fluid-structure interaction is a class of multiphysics where the coupled systems involved are fluid dynamics and structural mechanics. The coupling is represented by interactions between deformable and/or moving structures and a surrounding and/or internal flow. Simultaneous presence of structures and fluids results in interaction surfaces between the two. At these surfaces both physical fields governing equations as well as boundary conditions needs to be satisfied simultaneously. The theory of fluid-structure interaction that follows is available in [17].

Procedures used to solve FSI problems numerically are often divided into monolithic and partitioned methods. In common for the partitioned methods is that the different domains governing equations are solved for separately in sequential order, in contrast to the monolithic approach where they are solved simultaneously.

In this project the partitioned approach is implemented. Partitioned methods is further divided into one-way and two-way coupling. The difference being the directions of information transfer at the interfaces. In one-way coupling information is only transferred from one of the physical fields to the other. While information is transmitted alternately in two-way coupling.

Information relevant for transfer is problem dependent but consists of quantities at the interfaces and can often be categorised into kinematic ($\boldsymbol{x}$) and traction ($\boldsymbol{h}$) conditions. Kinematic being the motion of the interface and traction the force balance, which can be formulated as:

$$\boldsymbol{x}_\Gamma^f(t) = \boldsymbol{x}_\Gamma^s(t),\ \ \dot{\boldsymbol{x}}_\Gamma^f(t) = \dot{\boldsymbol{x}}_\Gamma^s(t),\ \ \ddot{\boldsymbol{x}}_\Gamma^f(t) = \ddot{\boldsymbol{x}}_\Gamma^s(t) \tag{2.58}$$

$$\boldsymbol{h}_\Gamma^f(t) = \boldsymbol{h}_\Gamma^s(t), \quad \boldsymbol{h} = \boldsymbol{\sigma} \cdot \boldsymbol{n} \tag{2.59}$$

where f denotes the fluid side of the interface and s the solid side. In this project, two-way coupling would be incorporated as deformations calculated in the structural domain being transferred to the fluid domain and forces calculated in the fluid domain being transferred to the structural domain. The simplification of one-way coupling restricts the information transfer to only consist of deformation or force transfer.

Two-way coupling methods is further categorised as weak or strong coupling methods. Strong coupling methods implementing an iterative process solving the governing equations for the two domains several times until a converged solution that satisfies the interface condition is obtained. While for the weak methods the iterative process is excluded and the equations are only solved for once.

Regardless of whether weak or strong coupling is assumed, implementing a one-way coupling method reduce the computational resources needed as the information transfer between the fields is reduced.

2.7 Vibrations and Pressure Fluctuations

Vibrations are generally divided into Self-excited vibrations and forced vibrations. Self-exited vibration lack exciting forces and results in vibrations with the structures natural frequencies. Self-exited vibration will not be considered in this study. It is in most cases not a problem for industrial fans as the one studied in this project so much as for aircraft gas turbines and similar turbines in which the blades mass ratio is small $\frac{m}{\pi\rho b^2}$(m, mass of blade per unit length; ρ, fluid density; b, half-chord length) [18]. Forced vibrations are vibrations caused by time-varying disturbances applied to a system. To avoid resonance it is common practice to design the structure such that its natural vibration does not match the time-varying disturbances. In this project it is assumed that resonance is not a concern. The disturbances considered are blade pressure fluctuations resulting from the structures interaction with the fluid. During normal operating conditions, pressure fluctuations on blades are commonly caused by unsteady flow fields arising from upstream flow disturbances such as rotors and stators or inlet flow conditions [18]. The design evaluated in this project contains neither preceding guide vanes nor rotors, and the inlet flow field is not disturbed in any obvious way. Major pressure fluctuations are therefore not easily distinguished. Other possible causes for blade pressure fluctuations are vortex separation from the blade, secondary flows and pressure fluctuations in the turbulent blade boundary layer [19]. One study conducted on a centrifugal fan of similar design resulted in the conclusion that the pressure fluctuations on the blade is mainly a consequence of the blades cutting through a quasi stationary helical inlet vortex [2]. The study concluded that the fan rotation imposed a pre-swirl on the inflow which resulted in the formation of this inlet vortex.

2.8 Fatigue Estimation

Vibrations that cause cyclic loading are not uncommon in rotating machinery such as the fan considered in this project. The cyclic loading caused by vibrations can cause failure of a structure, also known as fatigue.

Fatigue is the weakening of a material caused by repeatedly applied loads. It can also be thought of as crack growth were a crack grows a little bit each time the load is applied. This is illustrated in Figures 2.4 & 2.5 where the time-varying load $\sigma(t)$ with amplitude $\Delta\sigma/2$ in Figure 2.4 causes the crack in Figure 2.5 to grow Δl. The nominal stress values causing crack growth can be much lower than the strength of the material. Therefore it is important to account for these fluctuating loads and not just the maximum nominal stress when designing a durable product.

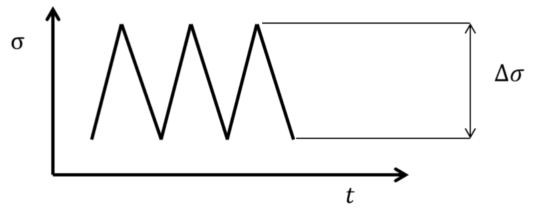

Figure 2.4: Time-varying stress in a component

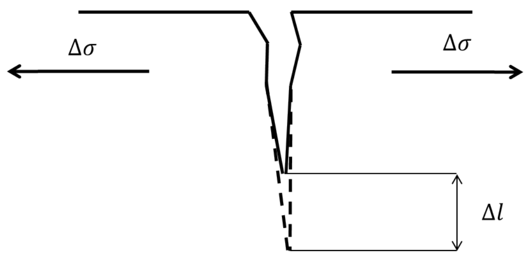

Figure 2.5: Crack in a component which grows Δl with a load cycle $\Delta\sigma$

Welds are often more prone to fatigue than other parts of a structure. When estimating fatigue for welds, tests are done to measure how many load cycles ($\Delta\sigma$) the weld can sustain before fracture. The tests result in an S-N curve as illustrated in Figure 2.6 where the stress amplitude $\Delta\sigma$ is written as a function of number of loads the structure can sustain, denoted N. Given a stress amplitude or stress range $\Delta\sigma$, the S-N curve gives an estimate on how many load cycles the weld can sustain. This procedure to estimate fatigue for welds is adopted in this project. In Figure 2.6 a decrease in slope can be noted after 10^7 cycles which indicates the very high cycle fatigue regime. The S-N curve used in this work for estimating fatigue is obtained from [20]. In summary, estimating the fatigue limit amounts to finding the stress range $\Delta\sigma$ in the structure which can possibly cause fatigue.

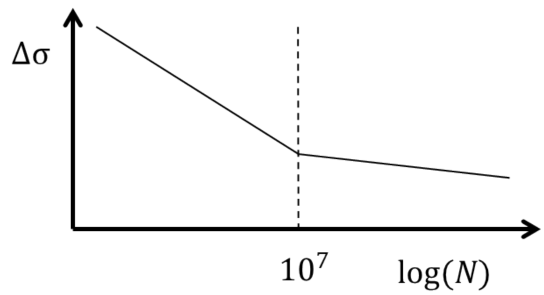

Figure 2.6: S-N curve for estimating the life length or fatigue limit of a component which is subject to repeatedly applied loads

3
Methods

In this chapter the simulation work flow and setup is outlined. First an overview of the method to simulate FSI is given as well as the operating conditions exerted on the fan. A description of the centrifugal fan together with the associated computational domain is given and the structural and fluid simulations are described in detail. Finally the procedure applied for data transfer between the fluid and solid domain is outlined.

3.1 Simulation Procedure

The method to simulate FSI was selected based on the assumption of weak interaction between the solid and fluid fields. Weak interaction means that aerodynamic forces on the structure has little impact on the deflections and reversely, the deflections of the structure has little impact on the flow field. This assumption allowed for separate structure and fluid analysis where they are simulated sequentially without iteratively passing information back and forth, thus reducing the computational requirements significantly.

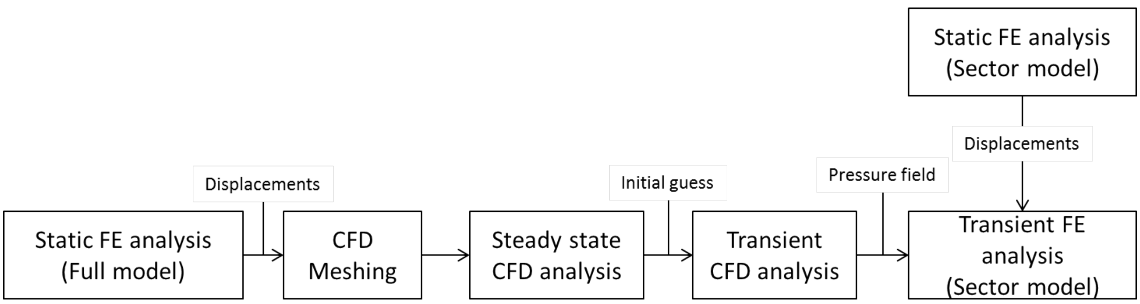

Figure 3.1: Flow chart describing the method of simulating FSI

The applied method for simulating FSI is outlined with the flowchart in Figure 3.1. The method can be described as one-way coupling in several steps. The deflection of the fan due to its rotation was assumed significant in comparison to those caused by aerodynamics loads. It was therefore of interest to investigate the effect of deflection due to centrifugal forces on the fluid flow. Displacements were solved for the full fan model while only accounting for the centrifugal load exerted on the fan due to the fan's inertia. This is shown as the first step in Figure 3.1. Displacements were transferred to the fluid domain mesh which was deformed accordingly. The deformed mesh was used to solve the unsteady fluid flow. The unsteady aerodynamic loads were applied to the sector model in a transient structural analysis and the time varying stress field was obtained. Displacements from the cyclic boundaries in a static analysis of the sector model were transferred to the cyclic boundaries in the transient analysis as boundary conditions, shown at the far right in the flow chart. This concludes the simulation procedure shown in Figure 3.1.

The simulations were performed for one set of operating conditions commonly used for the fan in standard operation. The rotational velocity was set to 1400 RPM, displacing 6 m^3/s of air in room temperature (22°C). The fluid was treated as air with parameters presented in Table 3.1. The fan consists of an Aluminium alloy with parameters presented in Table 3.2, the material was assumed linear elastic.

Table 3.1: Material parameters for air used in the fluid domain

Air (fluid)		
Density [kg/m^3]	**Kinematic viscosity [m^2/s]**	**Speed of sound [m/s]**
1.225	$1,7894 \cdot 10^{-5}$	343

Table 3.2: Material parameters Aluminium used in the solid domain

Aluminium (solid)		
Density [kg/m^3]	**Young's Modulus [GPa]**	**Poisson's Ratio**
2680	$70,5$	$0,33$

3.2 Geomtery & Computational Domain

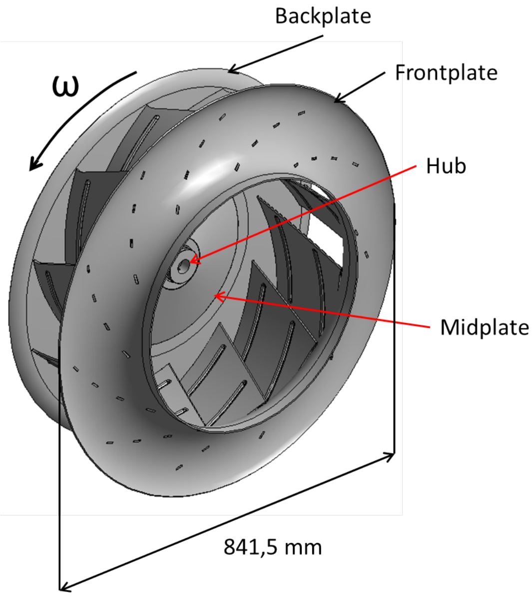

Figure 3.2: Centrifugal fan with labelled parts. $\boldsymbol{\omega}$ denotes the angular velocity of the fan

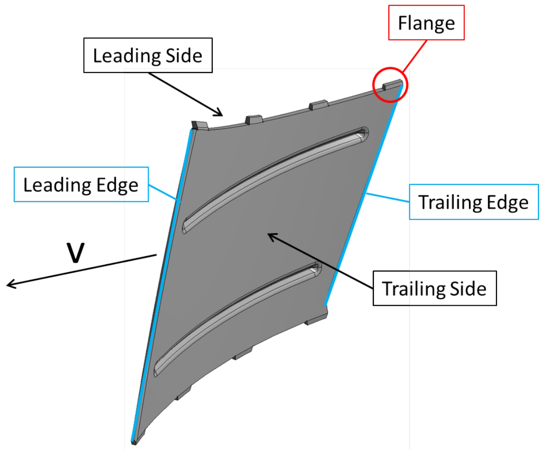

Figure 3.3: The blade with terminology of the blade explained. $\mathbf{v}$ denotes the instantaneous velocity of the blade

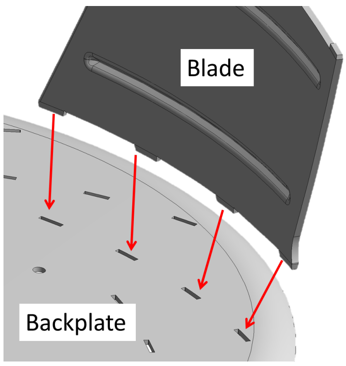

Figure 3.4: Illustration of the assembling of blade and Backplate

The centrifugal fan considered is shown in Figure 3.2 and one of the fan blades in Figure 3.3. The terminology of fan and blade, used in the remainder of this report, is defined in Figures 3.2 & 3.3. The fan consists of eleven backward curved blades and spans $841,5$ mm at its widest point. The blade features four flanges on top and bottom which fits into holes at the Back- and Frontplate, illustrated in Figure 3.4. The blades are fixed by laser welding the flanges to the plates resulting in the holes being filled up with material from the melted flange and surrounding plate. No material is added in the welding process. The welds on the blade were assumed most prone to fatigue, specifically the two welds adjacent to the leading edge. Midplate, Hub and Backplate are welded together as shown in Figure 3.5. Note the conical shape of the Midplate. All fan parts except the hub are manufactured from sheet metal which is stamped and bent. The blades features two slender indents along the chord which have the purpose of keeping the curved blades from returning to their initial shape.

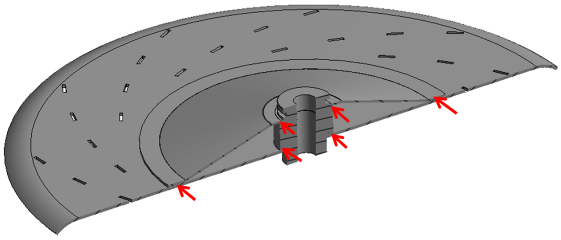

Figure 3.5: Cross section of Backplate, Midplate and Hub. Connections between the parts are indicated by red arrows.

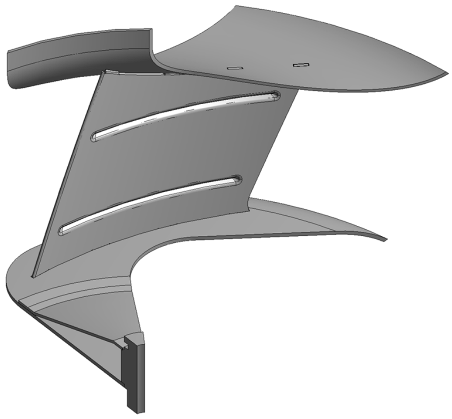

Figure 3.6: Sector model of the fan

Structural analysis was done on the whole fan and a sector model to take advantage of the cyclic symmetry of the fan and thereby reduce the computational demand. The sector model is shown in Figure 3.6 and makes up an eleventh part of the fan. Originally, the blades, Backlate, Frontplate, Hub, and Midplate were all separate parts. In order to obtain a reasonable approximation of the stress field in the vicinity of the welds, a sector model in which the blade, Backlate and Frontplate are merged was created. In summary, three geometries were used to perform structural analysis: A full fan model without merged parts, a sector model without merged parts and a sector model with Frontplate, blade and Backplate merged to one part. The sector models are referred to as sector A and sector B respectively.

The fluid domain was created to resemble the test chamber at Swegon with some simplifications. The fluid domain is shown in Figure 3.7 where the principal flow direction is indicated. Opposed to the structural simulations, no sector model was employed in the fluid simulations. Earlier studies suggest that the flow can not be modelled by a single sector with imposed periodic boundary conditions for a centrifugal fan [21, 2]. The domain consists of an inlet section and an larger outlet section. A nozzle is guiding the flow from the inlet section into the fan. The nozzle to fan interface is shown in detail in Figure 3.8, the downstream edge of the nozzle is mounted inside the fan with a small gap allowing for the fan to rotate and for air to pass. The mounting of the fan inside the test chamber with motor was not included i.e the fan was assumed fixed in space without mechanical suspension.

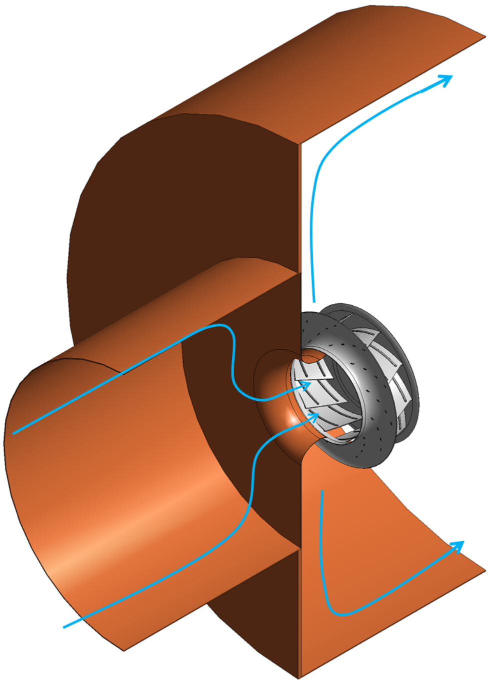

Figure 3.7: Cross section of the fluid domain with arrows showing the principal flow direction

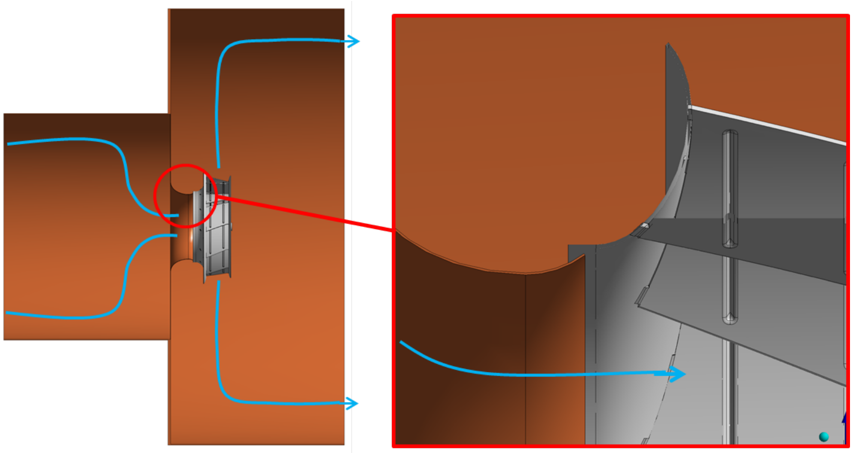

Figure 3.8: Side view of the fluid domain with a detailed view of the interface between nozzle and fan

Two main simplifications were done to the CFD model to avoid unnecessary detail which increase computational cost. As mentioned the blades are fit to the Back- and Frontplate by eight flanges, this fit is not perfect and leaves a small gap between blade and plate shown in Figure 3.9b. The gap was filled and the flanges were removed in the CFD model as shown in Figure 3.9a. The Hub and Midplate were also modified to reduce the level of detail, the modifications are shown by comparison in Figure 3.10.

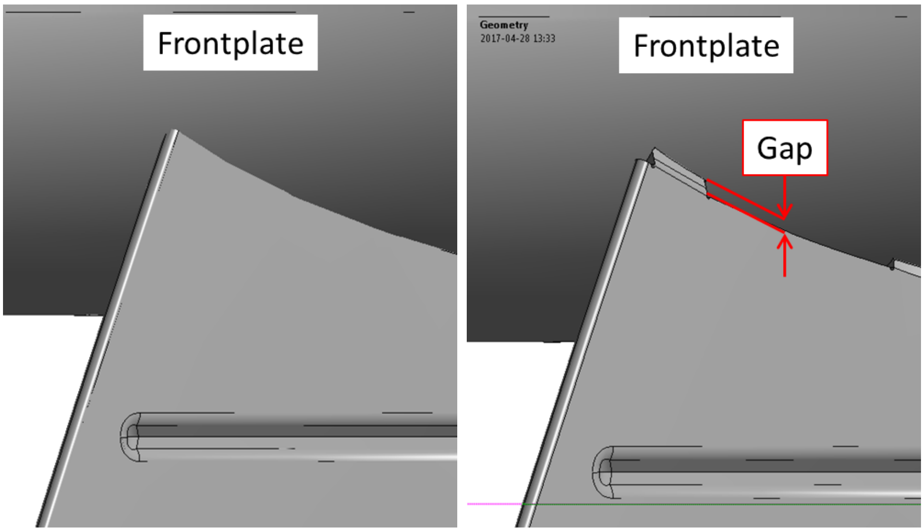

(a) CFD geometry **(b)** Original geometry

Figure 3.9: Showing modification done to the blade geometry in the CFD model

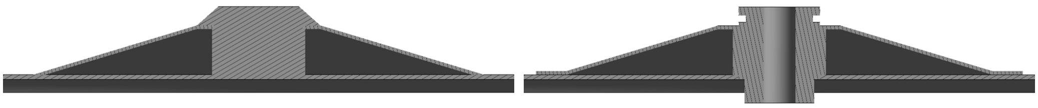

(a) CFD geometry **(b)** Original geometry

Figure 3.10: Cross section of the Hub showing modification done to the Hub geometry in the CFD model

3.2.1 Computational Grids

It is of interest to create computationally effective grids, providing adequate accuracy at a relatively low computational cost. To achieve this, the computational domains were split into different sections to enable local mesh sizing and meshing methods. Different mesh types were used and a mesh convergence study was performed for both structural and fluid simulations. ANSYS meshing were used to generate both FEM and CFD mesh. The meshing procedure for the fluid and solid domain is described in section 3.2.1.1 and 3.2.1.2 respectively.

3.2.1.1 Finite Element Mesh

The three different models for structural analysis mentioned in section 3.2, namely the full fan model, sector A and sector B were meshed independently. The meshes created for these models are described in the current section.

Advanced algorithms are implemented in the meshing software to automatically create high quality meshes with minimum user input. These automatic methods were applied to create the FE meshes. The algorithm base the local element size on properties of the geometry. Curvature of surfaces and gaps between geometric entities are examples of parameters which the algorithm base the local mesh size on. The algorithm also uses element shape checking to ensure mesh quality. In this study, jacobian ratio, skewness and element volume were used as shape metrics. The shape checking was set to *Nonlinear Mechanical* in ANSYS, described in [22]. Maximum element size and mesh type were used as input on top of the automatic meshing to obtain satisfactory meshes. Second order solid elements with three degrees of freedom per node were applied in all FE meshes.

Sector model A was meshed with tetrahedral elements with exception for the Midplate and Hub since they are axi-symmetric and very easy to mesh with hexahedrals, as shown in Figure 3.11a. Sector model A was only created to perform a mesh convergence study. Therefore, no effort was made to section the geometry for more efficient meshing. The coarsest mesh created for sector A is shown in Figure 3.11a where the maximum element size on the blade is set to 10 mm, and 15 mm for the other parts.

For sector model B, the blade was divided to enable hexahedral meshing of the blade as shown in Figure 3.11b. Maximum elements size was set to 4 mm. To resolve the stress field in the critical areas, a mesh with local mesh refinements in the vicinity of the two flanges situated closest to the leading edge was created as shown in Figure 3.12. The cyclic boundaries in the sector models were meshed to be conformal i.e the face mesh on the cyclic boundaries are identical. This is a requirement when performing cyclic symmetric analysis in ANSYS 17.0.

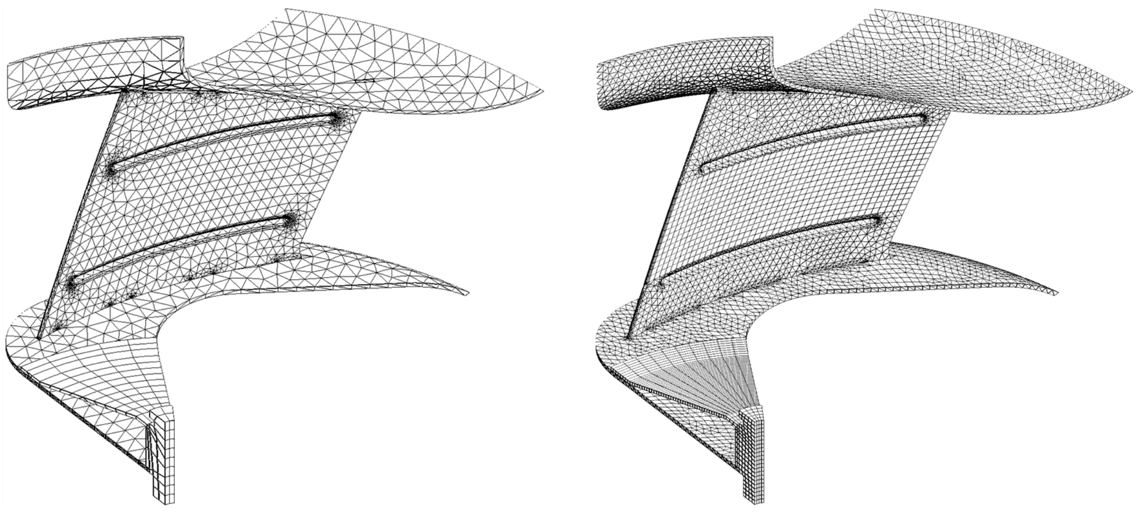

(a) Coarsest mesh for sector model A used for mesh convergence study

(b) Mesh for sector B

Figure 3.11: Comparison of the meshes for sector A and B

In the full fan model, Frontplate and Backplate were meshed with the *hex dominant method* in ANSYS [22], resulting in a mesh of hexahedral, pyramid and wedge elements. The blade was meshed as in sector B (see Figure 3.11b). The maximum element size of the different parts was set: Frontplate 4 mm, Backplate 4, 5 mm, Blade 3 mm, Midplate and Hub 5 mm. Meshing a large part of the full model with hexahedral elements greatly reduces the element count while preserving high element quality. To get a sense of how big the models are, element and node count is presented in Table 3.3.

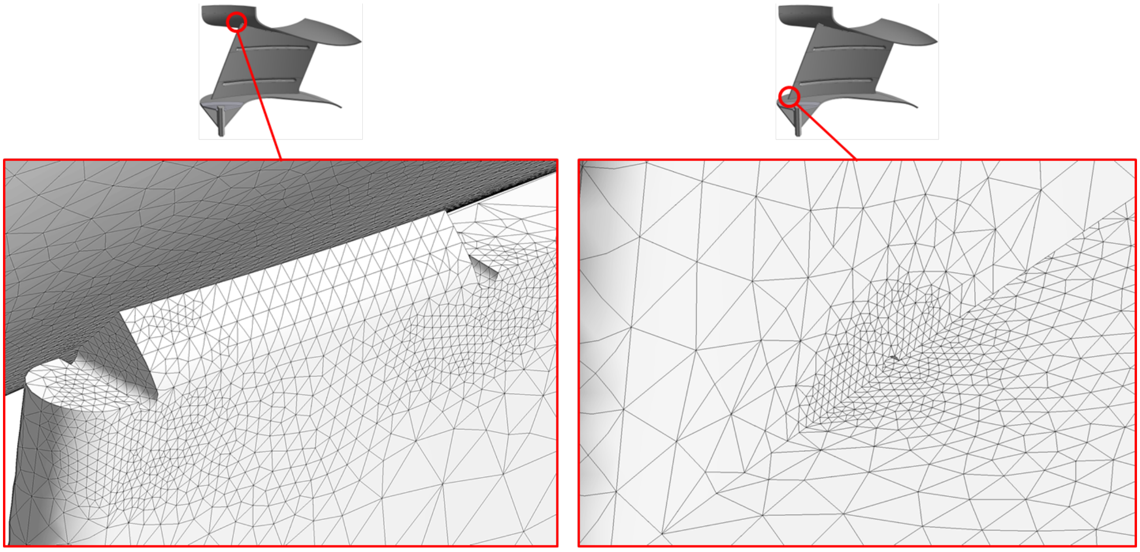

Figure 3.12: Local mesh refinement in sector B. The smallest elements are $0,4$ mm

Table 3.3: Node and element count for the FEM models

	Full Model	**Sector** A (Mesh Convergence)	**Sector** B	**Sector** B (Locally Refined)
Elements	727×10^3	34×10^3-540×10^3	60×10^3	198×10^3
Nodes	$1,6 \times 10^6$	55×10^3-883×10^3	125×10^3	321×10^3

3.2.1.2 Fluid Domain Mesh

The fluid domain was split into the different zones shown in Figure 3.13. The purpose of the split was primarily to enable rotation of the fan and secondarily to enable the creation of a hybrid grid where different cells and mesh topologies can be used in different parts of the domain. However, after the first simulations, results showed that the interfaces between zones influences the solution when different mesh types was used. The initial plan was to create an unstructured mesh with tetrahedral and triangular prism cells in the zones containing complex geometry i.e Rotating- and Middle-zone, and a structured mesh with hexahedron cells for the remainder of the domain i.e Inlet- and Outlet-zone. The final mesh was built with unstructured meshes containing tetrahedral and triangular prism cells in all zones.

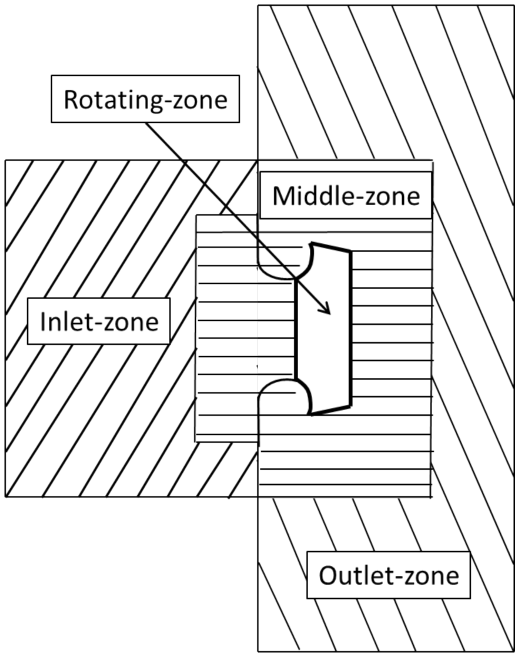

Figure 3.13: Cross-section sketch of the CFD domain with the different zones indicated by striped fields

Similar to the finite element mesh, the fluid domain mesh was built using algorithms creating high quality meshes with minimum user input. The significant differences from the FE mesh being how the cell size is determined and that the only criterion used for shape checking was the element volume. The cell size was determined by specifying a maximum cell size in all zones, as well as a specific cell size at all domain boundaries. The cells grow uniformly from the boundaries until they reach the maximum cell size in respective zone or does not meet the quality requirements.

The cell sizes specifications was determined based upon approximations of which areas that contain the largest gradients. It was concluded that the rotating zone and its near surroundings should be resolved using a smaller mesh size than the remainder of the domain. In the Rotating-zone the maximum mesh size is restricted to 15 mm and in the Middle-zone 30 mm. The fan surfaces have a size restriction of approximately 4 mm, with the exception of the leading and trailing blade edges, edges of the Backplate and Frontplate as well as in the gap between nozzle and fan. These areas have been refined additionally since they contain the largest gradients. A cross sectional view of the entire mesh with a zoomed in view of the Rotational-zone and the gap can be seen in Figure 3.14, the zoomed in areas are circled in red and blue respectively. The mesh in Figure 3.14 is the mesh before the displacements from the static structural analysis was transferred. The mesh consist of roughly eighth million cells, of which approximately 30% are located in the rotating-zone and approximately 40% are located in the Middle-zone. The resulting cell count on each blade is approximately 70 cells in the chordwise direction and 50 cells in the spanwise direction. The cell size was restricted to grow no more than 30% per cell.

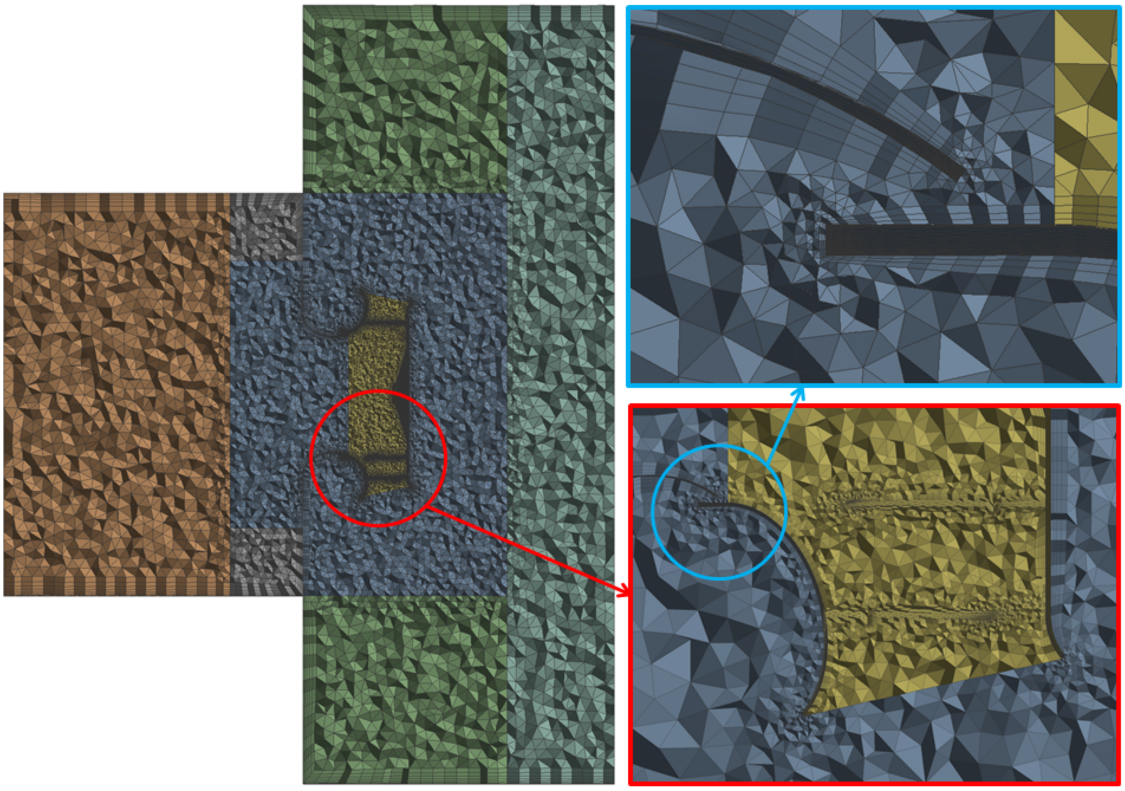

Figure 3.14: Cross-section of the CFD mesh with a zoomed in view of the Rotational-zone(red) and a further zoomed in view of the gap between nozzle and fan(blue)

Inflation layers were created at all walls to capture the large wall normal gradients of the flow. The Navier-Stokes equations as well as the chosen turbulence model, the SST model, is implemented in ANSYS Fluent to be y^+ insensitive. For the Navier-Stokes equations the law of the wall is implemented as a function of the local flow properties and mesh size. For the SST turbulence model, y^+ insensitive wall treatment means that turbulent transport equations are either integrated all the way to the wall, wall functions are implemented, or a blend of the two is used depending on the local flow properties and mesh size. The y^+ insensitive wall treatment seeks to reduce the requirement to fully resolve the turbulent boundary layer or to specify a specific y^+ value for all the wall adjacent nodes throughout the domain. In this study, all wall adjacent node y^+ values were lower than 150 and a minimum of three inflation layers were created. A larger number of inflation layers is preferable. Around 15 layers should ideally be situated inside the boundary layer according to [13]. However, a boundary layer resolution close to what was used during this study was implemented successfully simulating a fan with similar design, operating in similar conditions [23] and a minimum of three inflation layers was therefor deemed as adequate for this study. Information about turbulent boundary layers and y^+ can be found in section 2.5.4.

The cell quality is determined by computing orthogonal quality, aspect ratio and skewness in ANSYS Meshing, whose definitions can be found in [22]. All quality parameters stated below were calculated before the displacements from the static FEA were imposed on the CFD mesh. A quality check was performed in ANSYS Fluent after the displacements were transferred to ensure that the mesh quality did not significantly decrease.

Orthogonal quality ranges from zero to one, where values close to zero corresponds to low quality. The recommended minimum orthogonal quality according to Fluent [24] is $0,01$. The minimum orthogonal quality in the domain is $0,07$. Aspect ratio measures the stretching of the cells and can cause problems if to large. The Largest aspect ratio in the domain is 160. Skewness measures how close to an equilateral cell the considered cell is. Skewness ranges from zero to one, where values close one corresponds to low quality. Fluent recommends a maximum skewness not larger than $0,95$ [24]. The skewness is kept bellow $0,9$ in the whole domain.

3.3 Finite Element Analysis

Four finite element analyses were performed using ANSYS Mechanical 17.0:

1. Static analysis of the full fan model was performed to transfer displacements caused by centrifugal force to the CFD mesh. This analysis is the first step of the FSI method presented in the flowchart shown in Figure 3.1. Noteworthy is that, since the fan is cyclic symmetric, the same result can be obtained from a sector model. However, displacements could not be transferred from a sector model in structural analysis to a full model in CFD analysis.
2. Mesh convergence on sector A in order to ensure acceptable accuracy of the FE model.
3. Static analysis of sector B was performed to transfer displacements from the cyclic boundary to the transient analysis since the transient analysis did not support cyclic symmetric boundary condition.
4. Transient analysis of sector B (locally refined) was performed to account for the time varying loads from the fluid on the structure. The transient analysis was preceded by CFD analysis to obtain the aerodynamics loads. This analysis is the last step of the FSI method presented in the flowchart shown in Figure 3.1.

3.3.1 Centrifugal Load

The finite element analyses were performed in the rotating reference frame of the fan. This allowed for static analysis to be performed while accounting for inertia effects of the rotating fan i.e no relative motion of the fan and reference frame. When deriving Newton's law of motion in an rotating reference frame the centrifugal force appears which acts outwards in the radial direction of the circular motion. This technique of accounting for the fan rotation was applied in all the structural analyses. The centrifugal force can be written as a body force which can be inserted directly into Equation 2.8. The expression is stated as:

$$F_i = \rho \epsilon_{ijk} \epsilon_{klm} \omega_j \omega_l r_m \tag{3.1}$$

where ω_i describes the fan's planar rotation and r_i is the position with respect to the centre of rotation. ϵ_{ijk} is the alternating tensor used to represent cross product of vectors.

3.3.2 Boundary Conditions

To prevent rigid body motion the displacements were fixed at the centre hole of the Hub as shown in Figure 3.15. The fixed displacements simulate the fan being tightly mounted on a drive shaft.

A cyclic symmetry boundary condition was applied in the static structural analysis of the sector model. Applying cyclic symmetry, high and low boundary of the model were defined as in Figure 3.15. Cyclic symmetry implies constraining the displacements of each corresponding node on high and low boundary to be equal.

Since cyclic symmetry condition was not available for the transient analysis, displacements were prescribed on the cyclic boundaries from a static analysis. Hence, the displacements were fixed on the cyclic boundaries preventing any motion of those nodes. The deformations due to aerodynamic loads were assumed small compared to the deformation due to centrifugal force. Therefore, only centrifugal force was included in the static analysis performed to obtain the boundary displacements.

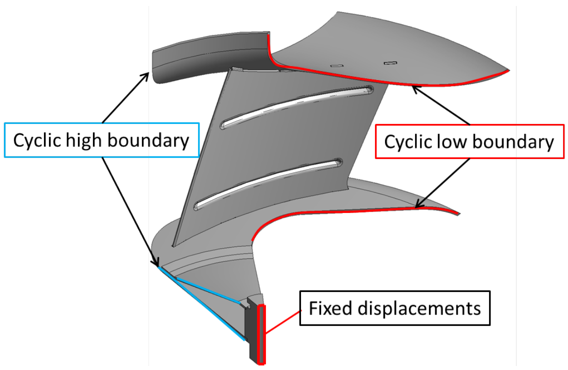

Figure 3.15: Boundary conditions on the sector model

3.3.3 Contact Definitions

Backplate, Hub and Midplate were fixed together at their contact surfaces indicated in Figure 3.16a using bonded connection formulated by the penalty method. Bonded connection does not allow any separation, penetration or sliding and can be thought of as parts being glued together. The blades were bonded to the Backplate and Frontplate by the flanges to the inside of the holes they are fit into, as shown in Figure 3.16c. The contact formulation on the flanges were set to MPC. As mentioned in section 3.2, the contact between flanges and holes does not apply to sector B as the parts were merged.

Friction contacts were also defined along the surfaces where the blades are not welded to the plates i.e between the flanges as indicated in Figure 3.16b. The friction is governed by a simple friction model: $F_f \leq \mu_f F_N$ where F_f and F_N denotes the friction force and normal force respectively, and μ_f is the coefficient of friction. The Coefficient of friction was set to 0,2

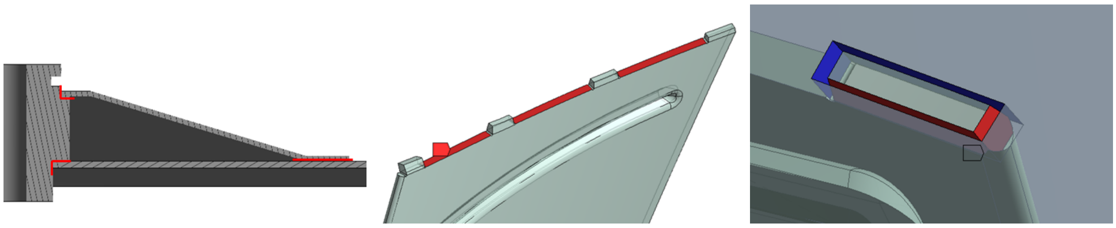

(a) Contact surfaces of Hub, Midplate and Backplate indicated with red lines

(b) Frictional surfaces on blade indicated by red

(c) Bonded contact between flange and plate hole, blue surface is bonded to red

Figure 3.16: Illustration of the different contact surfaces

3.3.4 Mesh Convergence

The mesh convergence study was performed on sector A to ensure that the model behaves as expected and can produce accurate results. Static FEA was run on four meshes of different size and maximum deflection was the graphed versus elements size to evaluate convergence. Initial element size was set, denoted h_0, and divided by 2, 4 and 6 to obtain the four meshes. The convergence study was used as a benchmark to ensure acceptable mesh density.

3.3.5 Aerodynamic Loads

Static pressure from the fluid simulation was mapped onto each surface of sector model B for transient analysis. The mapping was done using profile preserving mapping algorithm described in [25]. The pressure loads are kept perpendicular to the surfaces at which they are applied as they deform during the analysis. The pressure was stepwise applied with an time interval of $2,381 \times 10^{-4}$ seconds which corresponds to the fan rotating 2°. Stepwise, meaning the mapped pressure profile is kept constant over the time step. The time interval is longer than what was used in the CFD simulation but deemed sufficient to capture the important frequencies based on frequency analysis of the pressure fluctuations (described in section 3.4). To initialise the transient simulation the time integration was turned off and the same pressure was applied in the two first time steps to avoid dynamic effects of the loads being put on instantly at $t = 0$. One revolution of the fan was simulated resulting in 180 time steps.

3.3.6 General Analysis Settings

Some general settings were common for all structural analyses. Large deflections were included meaning geometric nonlinearities were accounted for. The strain-displacement formulation allowed for large rigid body rotations described in section 2.1.2. Since the structure consists of plate-like components and is subject to centrifugal and pressure loads the nonlinear effects like spin softening and stress stiffening described in section 2.3 are relevant and included. Since nonlinearities exist in the models an iterative solver was required. The program was set to automatically decide how often the tangent stiffness matrix should be updated based on the nonlinearities present. Convergence criteria was set to *force convergence* which requires the difference between the internal force of the structure and the applied force to be small. The program calculates a reference value based on applied loads and multiplies it by $0,005$ to form the tolerance value for convergence.

3.3.7 Stress Analysis

The time varying stress was calculated at different points which are shown in Figure 3.17. All points are located in the vicinity of blade welds. Two points in the vicinity of the welds adjacent to the leading edge which were expected to be most prone to fatigue and two points in the vicinity of the welds adjacent to the trailing edge. These four locations on the blade were selected to see the effect of the pressure variations over the blade surface. The exact positions of the points were based on stress concentrations in the radii next to the flanges in order to analyse the worst case from a durability point of view. The maximum principal stress was calculated at each point at each time step. Maximum principal stress was of interest since it is often used as stress measure when estimating the life of a structural component [20]. The range of maximum principal stress and number of stress peaks were calculated to estimate whether the aerodynamic loads can affect the life of the fan.

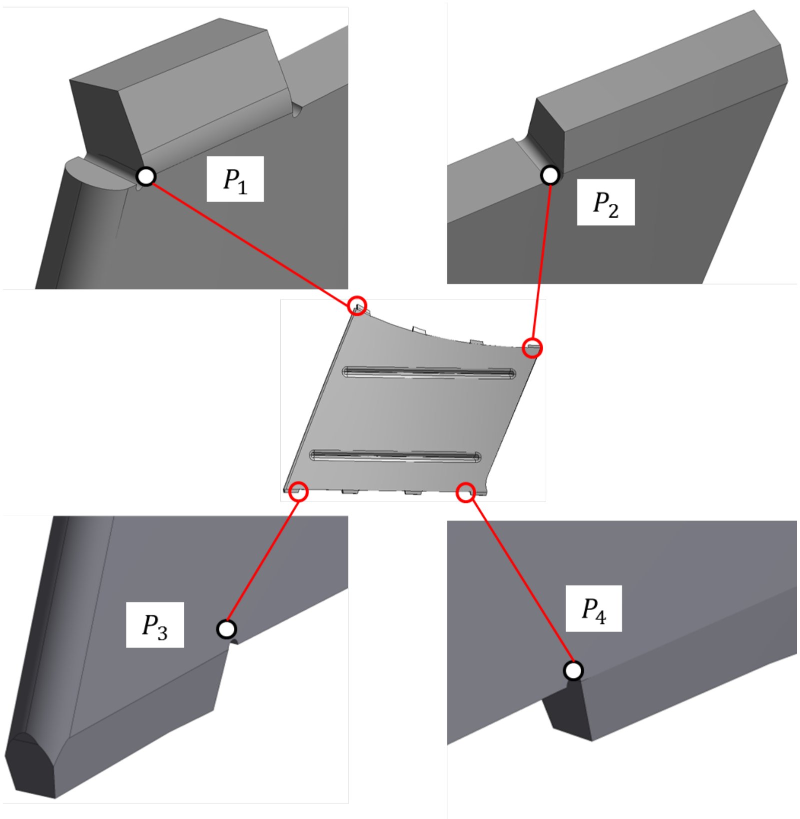

Figure 3.17: Locations of points where time dependent maximum principal stresses were analysed

3.4 CFD Analysis

All CFD simulations were performed in ANSYS Fluent 17.1. Steady state simulations were performed to conduct a mesh convergence study, compare turbulence models, validate simulation data with test results, and to obtain an initial guess for the transient simulations. Transient simulations were then performed to obtain pressure data that was later applied to the structure in FEA, but also to evaluate how large of an impact accounting for deformations due to centrifugal forces have on the blade pressure.

The mesh convergence study was done with the goal of obtaining a mesh that could be used to produce mesh independent results. The study was conducted by running a steady state simulation and measuring the pressure increase over the fan for five meshes with different cell count. The cell count was controlled by reducing the cell size with a constant factor throughout the entire domain. In this way the cell distribution was kept fairly constant for the different meshes. The study was performed on the undeformed fan. It is also desirable that the results does not strongly depend on the chosen turbulence model. A comparison of the pressure increase over the fan obtained using two different turbulence models was therefore conducted. The SST and Realizable $k-\epsilon$ models were compared. To validate the accuracy of the simulation, the pressure increase over the fan obtained trough simulations was compared to experimentally obtained data. The results were compared for four different mass flows with associated rotational speeds.

In the transient simulation, static pressure was sampled for each time-step on all surfaces associated with a selected fan sector, the same sector as used in FEA. Additionally, several sampling points on one fan blade were used to collect pressure data to analyse the time dependence of the pressure. To evaluate when the pressure fluctuations on the blade started to exhibited a periodic behaviour, the pressure on the sampling points was used to calculate the sample autocorrelation. When the pressure exhibited a periodic behaviour the flow was assumed fully developed and the period of the fluctuations was used as simulation time span for the transient FEA. The behaviour of the fluctuations was investigated in graphs of pressure versus time and pressure amplitude versus frequency. Fast fourier transform (FFT) was used to transform the pressure data from the time domain into the frequency domain. In the frequency domain, the part of the frequency spectrum containing the largest amplitude fluctuations were noted and used to determine an adequate time step to implement in the transient FEA. Transient simulations were performed on both the undeformed and deformed fan geometry to evaluate how the deformation due to centrifugal loads affects the pressure on the blade surfaces. An overview of all CFD simulations is presented in Table 3.4. Numerical aspects related to CFD are presented in the following sections.

Table 3.4: Overview of all CFD simulations. The SST turbulence model is employed in all simulations except simulation No. 10

No.	Purpose	Rotational Speed [RPM]	Volume Flow Rate [m^3/s]	Time	Number of Cells [M]	Mesh
1	Mesh convergence	1400	6	Steady	2,6	Undeformed
2					4,3	
3					5,2	
4					13,0	
5	Mesh convergence, Transient initalization & Turbulence model comparison	1400	6	Steady	8,2	Undeformed
6	PQ-curve	1378,6	4,4	Steady	8,2	Undeformed
7		1378	5,12			
8		1378	5,64			
9		1378,4	6,18			
10	Change of Turbulence model to realisable $k - \epsilon$	1400	6	Steady	8,2	Undeformed
11	Transient initialization	1400	6	Steady	8,2	Deformed
12	Gather pressure data for FE analysis & Mesh comparison	1400	6	Transient	8,2	Deformed
13	Mesh comparison	1400	6	Transient	8,2	Undeformed

3.4.1 Governing Flow Equations

The flow was treated as incompressible which usually is a valid assumption when the mach number is less than 0,3. The maximum mach number in the simulations was approximately 0,2. Heat transfer was not considered and since the flow was treated as incompressible, the energy equation did not need to be solved.

To be able to simulate the turbulent flow with the available computational resources, the time averaged flow equations (2.30 & 2.31) were solved which requires turbulence modelling, see section 2.5.1 and 2.5.2. A number of more or less complex turbulence models exists. The SST turbulence model was used in all simulations during this study, with exception for the turbulence model comparison case in which the Realisable $k - \epsilon$ model was implemented. The SST model is a well tested and often implemented turbulence model that initially was developed for aeronautic applications with focus on being able to accurately predict flows containing adverse pressure gradients, which are present in the studied flow. The model is described in section 2.5.2.1, model validation is available in [26] and studies similar to the present one in which the SST $k-\omega$ turbulence model have been implemented are found in [23, 27].

The flow equations are nonlinear and coupled to one another. It is common to decouple the Navier-Stokes equations from the continuity equation and to solve them sequentially in an iterative loop. In this way the memory usage is decreased but the iterative loop need to converge resulting in solving the equations several times, potentially increasing the simulation time. For the simulations performed in the current study the memory usage was not a limiting factor and a coupled solution algorithm was implemented. More information about the coupled algorithm can be found in [13].

3.4.2 Fan Rotation

While a majority of the fan is located in the rotating-zone, some of the fan surfaces are located in the middle-zone, which is shown in Figure 3.18. These surfaces are axi-symmetric and can therefore be modelled as rotating boundaries with no-slip boundary condition. In the Rotating-zone different model procedures were used in the steady state and transient simulations. For the steady state simulations the rotation was modelled by applying a rotating reference frame in the Rotating-zone, this method is known as *frozen rotor approach* and is described in section 2.5.5. For the transient simulation the rotation was instead modelled using the sliding mesh method, resulting in a spatial movement of the mesh each time step. The sliding mesh method is described in section 2.5.6.

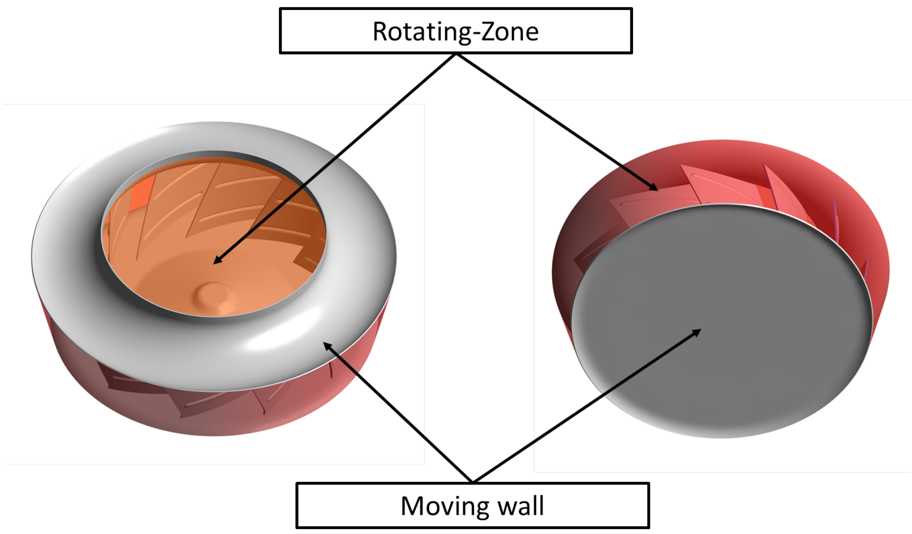

Figure 3.18: Fan geometry with the rotating-zone visualised in red and fan surfaces located outside the rotating-zone labelled as moving walls

3.4.3 Boundary Conditions

Boundary conditions were set to replicate the fans normal operating and testing conditions. Mass flow was specified at the inlet and static pressure at the outlet. Walls are modelled as no-slip surfaces, both rotating or stationary, see 3.4.2. Turbulent intensity and length scale were adopted as boundary conditions for the turbulent quantities both at the inlet and outlet. The intensity and length scale are approximated as:

$$I = 0.16(Re_D)^{-1/8} \qquad \text{(Turbulent intensity)} \tag{3.2}$$

$$l = 0.07D(C_\mu)^{-3/4} \qquad \text{(Turbulent length scale)} \tag{3.3}$$

where Re_D is the Reynolds number based on the inlet/outlet diameter, D is the inlet/outlet diamater and $C_\mu = 0,09$ is a model constant. Equation 3.2 estimates the turbulent intensity at the core of fully developed duct flows and Equation 3.3 estimates the length scale in fully-develpoed duct flows [24]. All boundary conditions are presented in Table 3.5.

Table 3.5: Summary of boundary conditions for the CFD simulation

Boundary	Type	Value
Inlet	Mass-flow Inlet	7,35 [kg/s]
Outlet	Pressure Outlet	0
Fan-walls Rotating Frame	No-slip Surface	-
Fan-walls Stationary Frame	No-slip Moving Surface	1400 [RPM]
Walls (excluding fan walls)	No-slip Surface	-
Inlet Turbulence	Intensity & Length Scale	I=3,29 l=0,705 [m]
Backflow Turbulence	Intensity & Length Scale	I=3,57 l=1,36 [m]

3.4.4 Discretisation

Discretisation schemes have been chosen based upon recommendations from ANSYS regarding rotating machinery which can be found at ANSYS customer portal [28]. Spatial discretisation was performed using both second and first order schemes. A second order upwind scheme was used to discretise momentum. For pressure a second order central difference scheme was used. The turbulent quantities was discretised using a first order upwind scheme. Temporal discretisation is performed using a second order implicit scheme. An implicit scheme brings the possibility of increased time steps as the grid size does not determine the maximum time step trough the CFL number as it does for explicit schemes [23]. The same discretisation schemes have been applied successfully in ANSYS fluent during a similar study in which the pressure fluctuations in a centrifugal fan were of interest [23].

3.4.5 Time-Step & Convergence Criterion

The steady state simulation was considered converged when the inlet pressure as well as all of the available globally scaled residuals in ANSYS Fluent stabilised. The globally scaled residuals were residuals of continuity, velocity and turbulent quantities (see [13] for definitions). When the solution was considered converged, the residuals of velocity and turbulent quantities reached a value below 10^{-3} and the residual of continuity reached a value below $2 \cdot 10^{-2}$.

While taking limited computational resources into account, the time step was determined based upon studies made on similar fans, convergence rate and frequency resolution. A time step corresponding to roughly 1° rotation per time step has been used successfully during similar studies, performed with Fluent, in which pressure fluctuations in centrifugal fans are of interest [23, 27, 29, 30]. The convergence criteria used in [23, 27, 29, 30] had been set in terms of the globally scaled residuals available in ANSYS Fluent and the solutions was considered converged when each one of the residuals had reached a certain residual limit. This residual limit was in [23, 27, 29, 30] set to a value between 10^{-6} and 10^{-4}, different values used in different studies. To determine an adequate residual limits for the transient simulations performed in the present study, different values were tested and the pressure field was analysed. It was observed that the blade pressure changed a few pascals as the residual limit was decreased from 10^{-4} to 10^{-5}. It was also observed that the computational time increased drastically when the limit was further reduced while the pressure field did not change considerably. The solution was therefor considered as converged when the globally scaled residuals reached bellow 10^{-5}, which was used as convergence criterion for all transient simulations.

Different time steps corresponding to a rotation in the vicinity of 1° were tested with the chosen convergence criterion. It was noted that the computational time needed to reach convergence did not increase significantly as the time step corresponding to 1° was reduced to $0,5°$. Since a shorter time step allows for higher frequencies to be resolved as well as decreases the risk of divergence, the shorter time step $\Delta t = 5,952 \cdot 10^{-5}$[s] corresponding to $0,5°$ was used.

3.4.6 Sampling Points

To evaluate the pressure fluctuations on the blade surface, 18 small squares were created on one of the blades to sample the pressure point wise. As the squares are not strictly points but surfaces containing approximately two cells each, the pressure was taken as the average over the square. Nine squares were created on each side of the blade (leading and trailing side) as shown in Figure 3.19. Each square has a corresponding square on the other side of the blade. The L notation of the squares in Figure 3.19 refers to the leading side. The points on the trailing side are denoted T with the same logic for the subscripts, subscript 11 located at the upper corner close to the leading edge, 13 close to the trailing edge and so forth. The pressure was sampled from every time step on the squares.

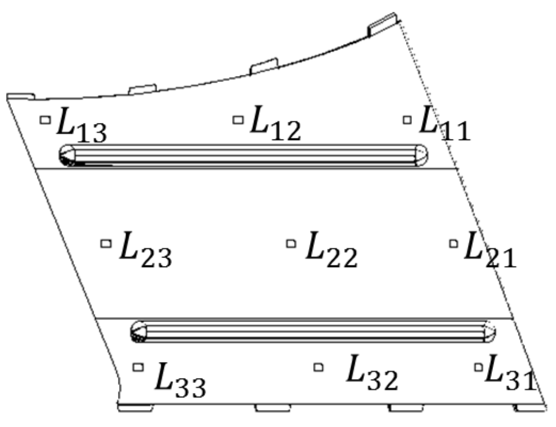

Figure 3.19: Pressure sampling positions on the leading side

3.4.7 Mesh Deformation

Displacements were transferred from the structural analysis to the fan surfaces in the CFD mesh. Deformation of the CFD mesh was done using mesh smoothing, meaning no new nodes were created but existing nodes were moved. The mesh deformation is done in Fluent with the *linearly elastic solid* smoothing method. The volume mesh was treated as a linearly elastic solid with prescribed displacements at the boundaries where displacements were received. The displacements at the interior nodes were then solved for using finite element analysis. The equations for a linearly elastic solid with prescribed displacements can be said to only depend on Poisson's ratio which is the only material parameter available as user input for this method [24]. Poisson's ratio was set to $0,45$ for the smoothing method.

3.5 Data Transfer

There were four occurrences of data transfer while performing this FSI simulation as shown in the flow chart of Figure 3.1 in the beginning of this chapter. The data transfers were handled differently which is described here. The transfer of displacements from the FEM model to the CFD mesh was performed using ANSYS *System Coupling* tool available in ANSYS Workbench. Source surfaces were selected in the FEM model and target surfaces in the CFD model. A source surface could only be transferred to one target surface and vice versa, therefore all surfaces in the CFD model must have a corresponding surface in the FE model. Since the fan is cyclic symmetric, the aim was to perform all FE analyses on the sector model but it was not possible using the *System Coupling* tool. Using the *System Coupling* tool, static FEA and CFD mesh deformation were performed in one analysis step without any user interaction during the procedure. When the displacements were transferred successfully and the CFD mesh deformed, the mesh was exported to be used in other analyses. The Workbench setup to perform transfer of displacements to the CFD mesh can be found in Figure A.1.

The transfer of data from steady state CFD to transient was simply done by loading the data for each cell into the transient analysis since they were performed on the same mesh. The pressure was sampled for each node on the sector imprint for each time step and printed to text files where information about the node coordinates and the pressure was stored. The viscous wall stress was neglected as it was deemed small compared to the static pressure. The text files were read into the transient structural FEA using the *External Data* module in ANSYS Workbench. This data transfer was done externally and required user interaction. The nodes at which the pressure is sampled rotates relative to the coordinate system in the CFD analysis, but the transient FE was solved in a coordinate system which is stationary relative to the fan. Therefore each pressure node was rotated to match the FEA coordinate system by a small Python script implemented in the *External Data* module in ANSYS Workbench. The script can be found in the appendix A.1.

The transfer of boundary displacements from the static to transient FEA was done directly in ANSYS Workbench by connecting the static analysis to the transient and selecting the high and low boundary in the transient analysis. The method of transferring the displacements to the cyclic boundaries is the same as performing sub modelling. The workbench setup to transfer data between analyses can be found in the appendix A.2.

4
Results

In this chapter the entire simulation outcome is presented and explained. The chapter is divided into a section covering finite elements analysis and a section converging computational fluid dynamics.

4.1 Finite Element Analysis

The structural analysis results are presented and explained in this section. The results are mainly divided into static results and transient results. The displacement field from static analysis is presented together with the mesh convergence study. The stress field obtained from transient analysis is analysed and presented with emphasis on the stress range close to welds on the blade. A crude estimate of the fatigue limit with respect to the obtained stress range is presented to evaluate the necessity of including the fluid pressure in fatigue estimation. One should keep in mind that the transient structural analysis is preceded by CFD analysis to obtain the aerodynamic loads. The CFD results are presented in section 4.2.

4.1.1 Static Deformations

The most interesting result from the static analysis of the full fan was the deflection since it served to provide deformations for the CFD mesh. The maximum deflection is labelled at the leading edge in the total deformation contour shown in Figure 4.1. The blades attain a curved shape outwards while the fan rotates and thereby the fan is somewhat compressed in the axial direction. Keeping in mind that the deformations are scaled with a factor 32 in Figure 4.1 the deformations due to rotation are very small in comparison to the dimensions of the fan. Results of the mesh convergence study, described in section 3.3.4, is presented in Figure 4.2. The maximum deflection achieved in the mesh convergence study is $0,974$ mm. Compared to the maximum deflection of the full model in Figure 4.1 at $0,968$ mm the deflection in the full fan model is deemed satisfactory.

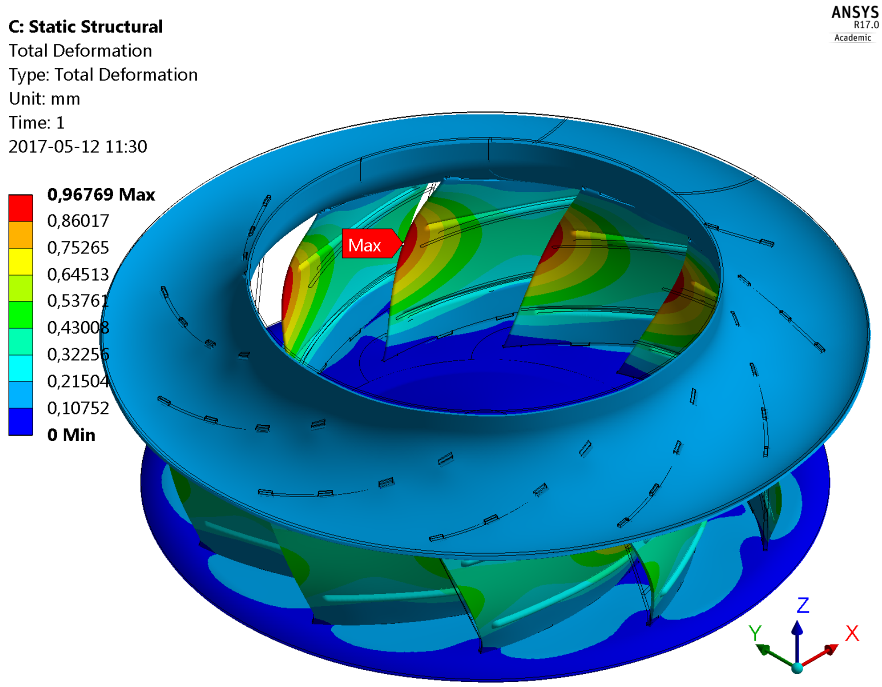

Figure 4.1: Contours of total deformation plotted on the deformed shape of the full fan model. A wire-frame of the undeformed shape is plotted on top. The deformations are scaled by a factor of 32 for visualisation of the deformed shape

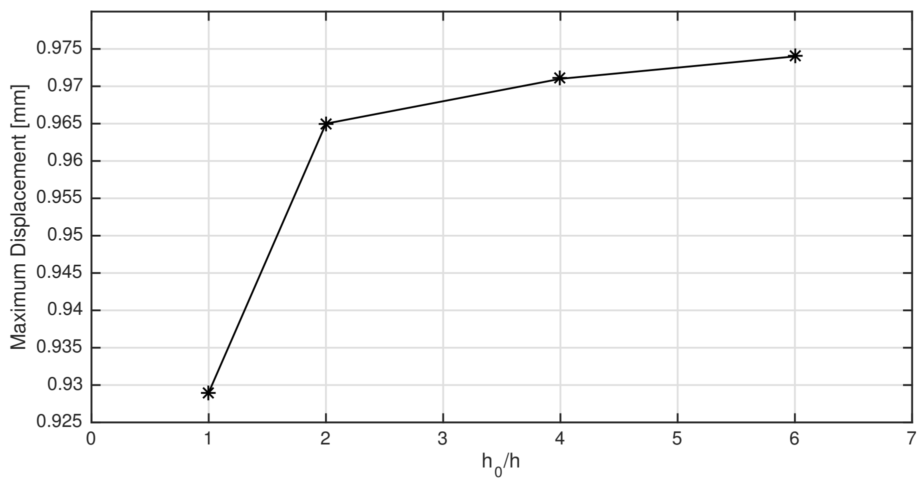

Figure 4.2: Maximum displacement for four meshes with different resolution. h_0 is the element size used for the coarsest mesh

The static analysis on sector B for transferring boundary displacements to the transient analysis gave similar results to the full model with a maximum deflection of $0,952$ mm. Note that blade, Back- and Frontplate are merged in sector B as opposed to sector A used for the mesh convergence study. To evaluate the assumption of neglecting the effect of aerodynamic loads on the cyclic boundary in the transient analysis, comparison of displacements on the cyclic boundary with and without aerodynamic loads is done. The comparison is made by presenting the mean and maximum difference in total displacement (in mm) over all nodes on the cyclic boundary. Let $\mathbf{A}_{aero}$ be the vector of total displacements in each node on the cyclic boundary with pressure from CFD analysis applied, and $\mathbf{A}$ be the vector of total displacements without pressure:

$$\text{mean}(|\mathbf{A}_{\text{aero}} - \mathbf{A}|) = 2,1 \times 10^{-3} \text{ [mm]} \tag{4.1}$$
$$\max(|\mathbf{A}_{\text{aero}} - \mathbf{A}|) = 7,9 \times 10^{-3} \text{ [mm]} \tag{4.2}$$

The difference in total displacements on the cyclic boundary by adding aerodynamic loads are in the order of micrometres.

4.1.2 Aerodynamic Loads

The result of pressure mapping is shown in Figure 4.3. As expected the pressure is gradually increasing over the fan from inflow to outflow. The average pressure on the leading side is higher than trailing side, resulting i a torque acting opposite to the fan rotation. The resulting torque caused by the pressure loads on the blade is $3,14$ Nm. This calculated torque can be compared to a measured torque on the drive shaft from a test with similar operating conditions (flow rate of $6,18$ m^3/s and angular velocity of 1378 RPM), which results in a torque of $3,25$ Nm. The pressure maintains its main profile as in Figure 4.3 throughout the revolution. The resolution of the pressure field depends on the FE mesh and the CFD mesh since they are differently sized in different regions. The largest difference in total displacement by applying the pressure in addition to the centrifugal load is $0,01$ mm, similar to the values calculated in Equations 4.1 & 4.2

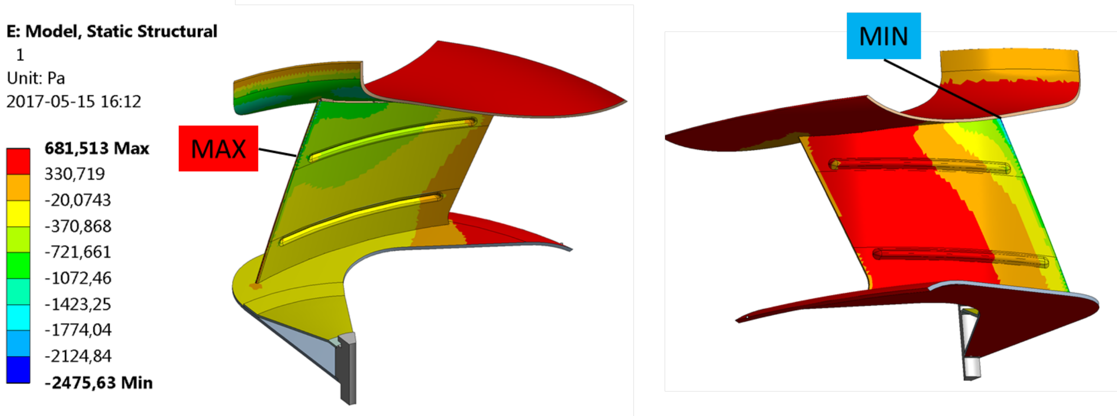

Figure 4.3: Contour of the mapped pressure on the sector model at the end of revolution seven. Trailing side (left) has a lower average pressure than leading side (right)

4.1.3 Stress Analysis

The effects of centrifugal load on the stress field can be observed in Figure 4.4 where the leading side is in compression and the trailing side in tension because of the outwards bending of the blade visible in Figure 4.1. The stress state exhibited in Figure 4.4 is representative for all flanges on the blade. Since the leading side is in compression regardless of the aerodynamic loads, the stress variations are only examined close to the trailing side since compressive stresses are not likely to cause crack growth and eventually fatigue. Therefore, all points where stress is examined are located on the trailing side on the blade.

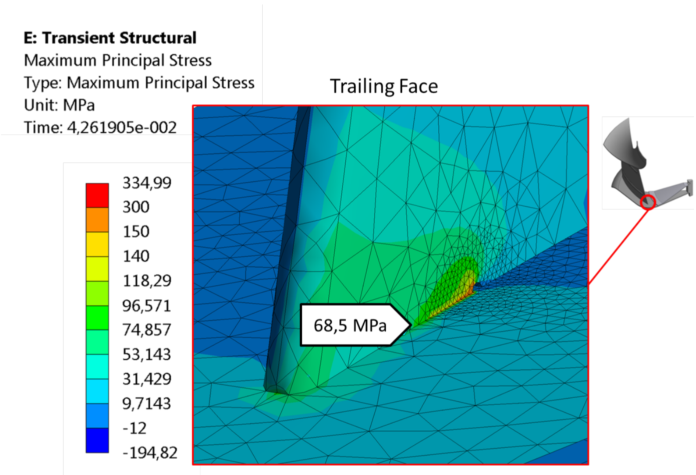

(a) Showing tensional principal stress at the trailing side of the weld

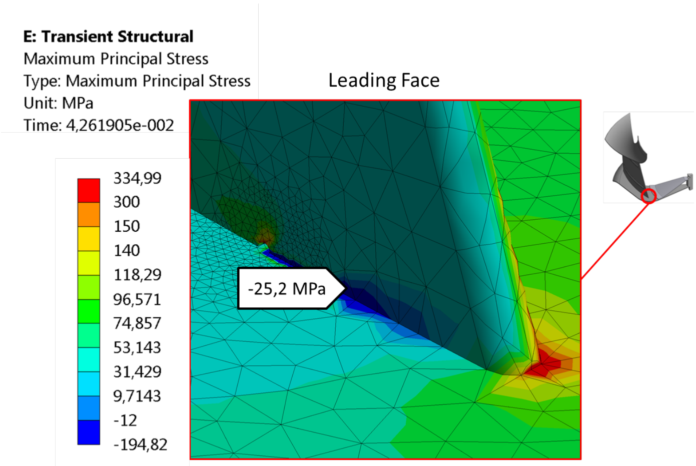

(b) Showing compressive principal stress at the leading side of the weld

Figure 4.4: Comparing maximum principal stress at the trailing and leading side of the weld joining Backplate and blade at the leading edge

The stress histories are evaluated at $P_1 - P_4$ which are located at stress concentrations, the locations are described in detail in section 3.3.7. The highest principal stress occurs on the surface of the solid, which is visible in the cross-sectional view in Figure 4.5 (Right), which is the case for all stress concentrations near the welds.

In Figure 4.6 maximum principal stress appears on the the right side of the flange in the radius, while the stress range is largest on the left radius. Therefore P_1 is located at at the left radius in Figure 4.6 since stress range is the determining factor when estimating fatigue. The stress reaches values over the yield limit for the material in stress concentrations in Figures 4.5 & 4.6 which is possible since a linear elastic material model is used.

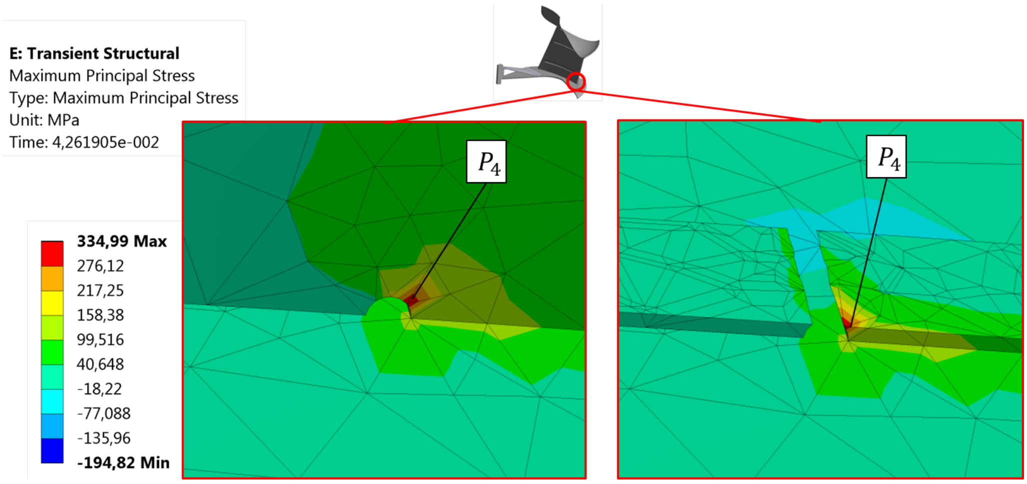

Figure 4.5: Close up of the stress concentration of P_4. A cut view is shown to the right to demonstrate that the stress is highest at the surface

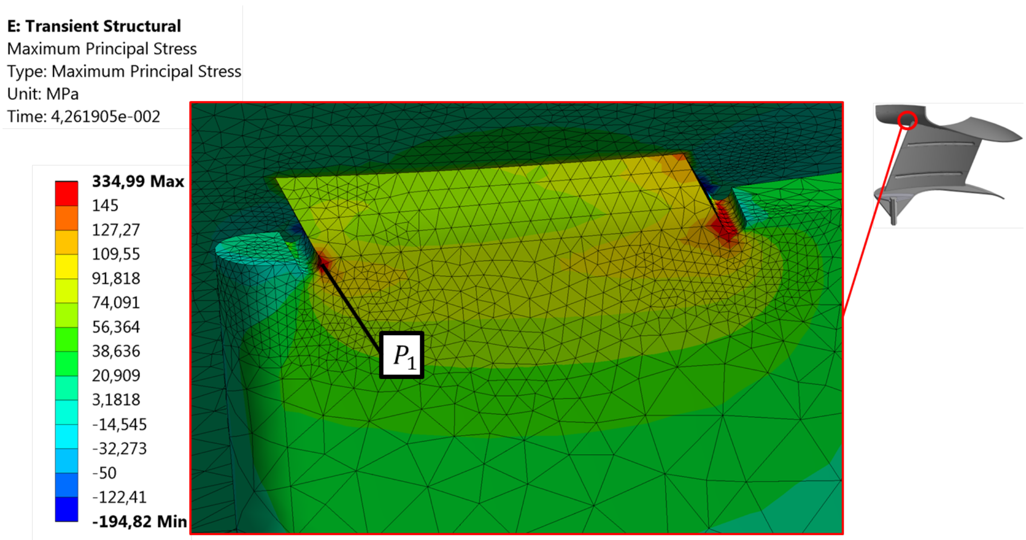

Figure 4.6: Close-up of upper flange at the leading edge, view from trailing side

The maximum principal stresses in $P_1 - P_4$ are plotted for one revolution in Figure 4.7. The maximum stress range over time, σ_R, and the number off stress peaks are written in each graph window of Figure 4.7. Comparing P_1 and P_3 to P_2 and P_4 i.e leading to trailing edge, difference can be noted in range and frequency. P_1 and P_3 have higher maximum stress range but fewer stress peaks. The highest value of σ_R is found at P_3 shown in Figure 4.7c because of a relatively low principal stress for the first time step which is not reoccurring. Noteworthy is that the stress variations due to the aerodynamic loads are a fraction of a percent compared to the mean value of the stress in the points P_1-P_4. A very crude estimate of the fatigue limit of the welds is made based on the methods and data in [20]. The number of cycles is calculated accordingly as:

$$N = 10^7 \times \left(\frac{\sigma_{10^7}}{\sigma_R}\right)^m \tag{4.3}$$

where σ_{10^7} is the stress range, in MPa, at which the fatigue limit is 10^7 cycles, m is a constant which differs depending on fatigue regime. For stress ranges lower than σ_{10^7}, $m = 22$. Assuming the weld with lowest σ_{10^7} which is 7 MPa, i.e the weakest weld in terms of fatigue resistance presented in [20], and the highest σ_R which is $0,134$ MPa (from P_3) gives:

$$10^7 \times \left(\frac{7}{0,134}\right)^{22} \gg 10^{30} \tag{4.4}$$

The high number of cycles indicates that the fatigue estimation is a matter of ultra high cycle fatigue which is a area under development and outside the scope of this work.

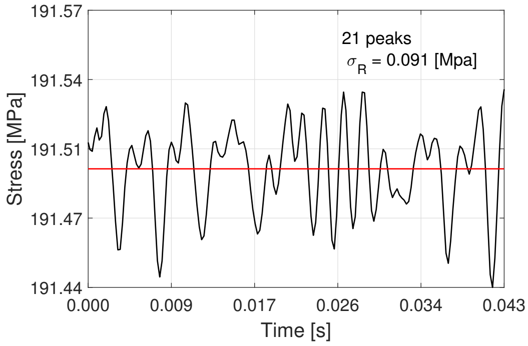

(a) Time history of maximum principal stress in P_1 (near leading edge)

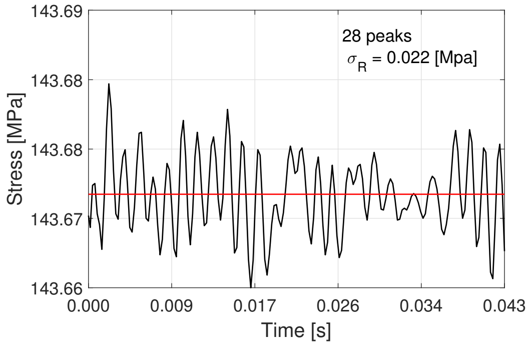

(b) Time history of maximum principal stress in P_2 (near trailing edge)

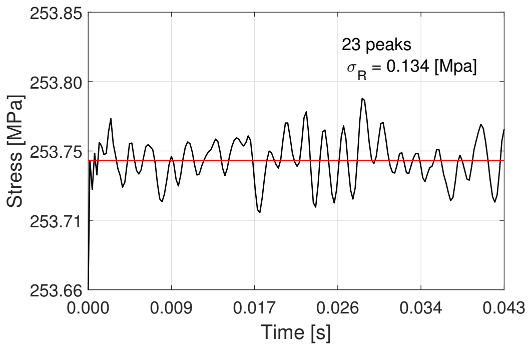

(c) Time history of maximum principal stress in P_3 (near leading edge). Note that the stress obtains its minimum magnitude, 253,66 [MPa], at the first time step.

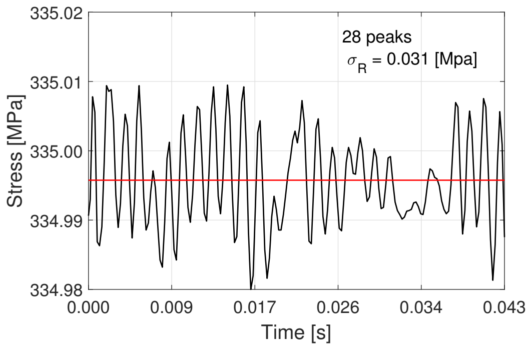

(d) Time history of maximum principal stress in P_4 (near trailing edge)

Figure 4.7: Time histories of the maximum principal stress in the sampling points $P_1 - P_4$ for one revolution of the fan. Mean stress over time is drawn in each graph (red horizontal line)

4.2 Computational Fluid Dynamics

The results obtained trough fluid simulations are presented and explained in this section. An overview of the simulations performed is available in Table 3.4. Verification of the simulation setup is presented in the form of a comparison against experimental results, a mesh convergence study and a comparison of turbulence models in section 4.2.1, 4.2.2 and 4.2.3 respectively. Analyses of the flow timescales trough autocorrelation and frequency analysis are presented in section 4.2.4 and 4.2.5. The impact of running the simulations on the deformed mesh is studied in section 4.2.6 and the flow field is visualised through hydrodynamical helicity, revealing interesting flow structures, in section 4.2.7.

4.2.1 Pressure-Flow Rate Curve

Figure 4.8 shows static pressure increase over the fan as a function of the volume flow rate. Data obtained from measurements at Swegon's test facility and data obtained through simulations 6-9 (in Table 3.4) is presented in the same graph. The results shows similar behaviour as the flow rate changes but it is noted that results obtained through simulations overestimates the pressure increase. Explicit values of the overestimate is presented in Table 4.1.

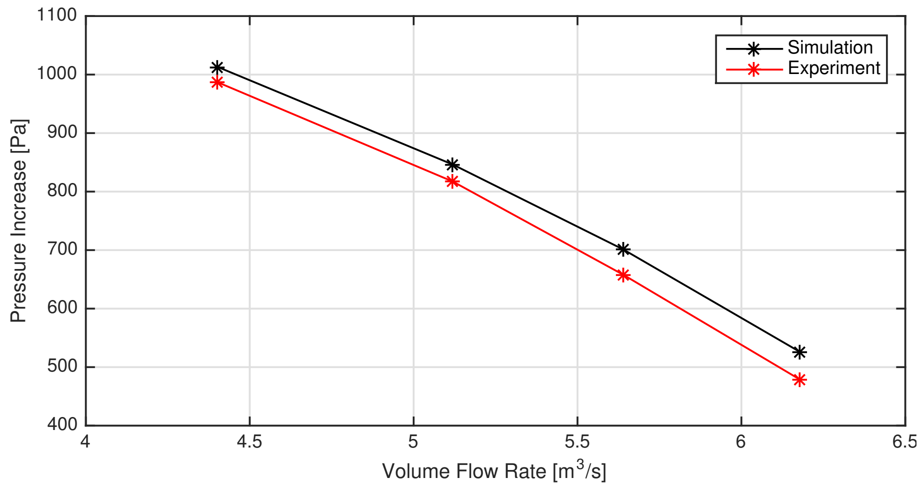

Figure 4.8: PQ-curves for the experimental and numerical results.

Table 4.1: Comparison between the PQ-curve obtained through experiments and numerical simulations.

Volume flow rate	4,2	5,12	5,64	6,18
Pressure increase overestimate [Pa]	26	29	43	47
Pressure increase overestimate [%]	2,7	3,6	6,6	9,9

4.2.2 Mesh Convergence

The pressure increase over the fan obtained in simulations 1-4 (Table 3.4) are presented in Figure 4.9. h is the cell size and h_0 refers to the initial cell size for an unrefined mesh. Since the cell size is not uniform, h is measured locally. Between the two finest mesh sizes, $h/h_0 = 2$ and $h/h_0 = 2,7$, the change in pressure increase is approximately 0,3 %, which is considered to be sufficiently small for mesh convergence. A mesh cell size corresponding to $h/h_0 = 2$ was used to produce all results that follows. It translates into a cell count of approximately eight million. Details about the mesh can be found in section 3.2.1.2

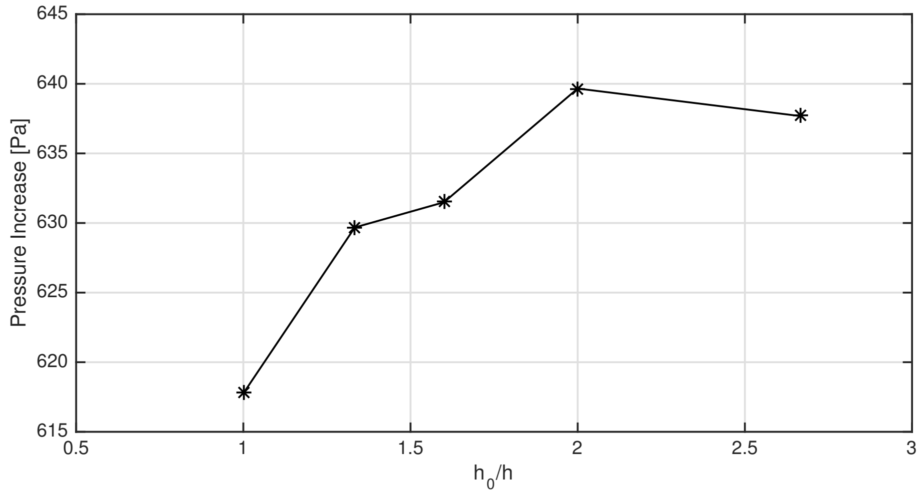

Figure 4.9: Pressure increase for five meshes with different mesh resolution. h is the current cell size and h_0 refers to an initial unrefined mesh.

4.2.3 Turbulence Model Comparison

The pressure increase over the fan for two different turbulence models is presented in Table 4.2. The results are obtained trough simulations 5 and 10, see Table 3.4. It is concluded that the change of turbulence model did not significantly alter the result.

Table 4.2: Static pressure increase over the fan for two different turbulence models

Turbulence Model	Pressure Increase [Pa]
SST $k-\omega$	639,6
Realizable $k-\epsilon$	636,5

4.2.4 Periodic Flow

To determine if the time varying pressure on the blade exhibits a periodic behaviour the pressure on the sampling points is used to calculate the sample autocorrelation, with a signal delay ranging from one degree to one revolution. The delay between the signals giving the highest correlation is calculated to one revolution. A periodic behaviour with the interval of one revolution is therefore assumed. With the aim of approximating how many revolutions that needs to be simulated before the pressure fluctuations are periodic, the autocorrelation between subsequent revolutions is calculated and presented In Table 4.3. The autocorrelation is calculated in each one of the eighteen sampling points, the presented value in Table 4.3 is the average of these. The autocorrelation lies in the range [-1, 1], where a value of 1 indicates perfect correlation. Between revolution six and seven the autocorrelation reaches a value of 0,95 and the blade pressure is therefore assumed periodic after revolution five $t = 0,214$ with a period of one revolution. This study was performed using pressure data sampled during simulation 12 in Table 3.4.

Table 4.3: Sample autocorrelation of the static pressure in the sampling points with a delay of one revolution and a total sample size corresponding to two laps.

Revolutions	1 & 2	2 & 3	3 & 4	4 & 5	5 & 6	6 & 7
Sample Autocorrelation	0,256	0,802	0,827	0,846	0,784	0,948

4.2.5 FFT

The fast fourier transform algorithm is implemented to transfer the static pressure data measured in the sampling points during simulation 12 (see Table 3.4) from the time domain into the frequency domain. This is done to distinguish the frequencies that has an insignificant contribution to the time domain signal and therefore can be excluded in structural simulations. As can be seen in Figure 4.10 the frequencies above approximately 1000 Hz have relatively low amplitudes compared to the lower frequencies. The Nyqvist theorem, determining the sampling speed required to avoid aliasing, states that the sampling frequency should be at least twice the highest frequency contained in the signal. Resolving frequencies up to 1000 Hz will therefore require a sampling speed of at least 2000 Hz, which translates to approximately 90 samples per revolution with a rotational speed of 1400 revolutions per minute. A sampling speed twice as fast was chosen to increase the resolution further, resulting in 180 samples per revolution being transferred to the structural simulations.

When performing frequency analysis of pressure data in turbomachinery applications, the largest amplitudes are often found at the blade passage frequency and its harmonics. The blade passage frequency in the studies case is 256,7 Hz. It is noted from Figure 4.10 that it's amplitude is not larger then the ones found at the surrounding frequencies. The reason for this is that the blade rotates with the flow. For sampling points stationary in the domain, the amplitude at the blade passage frequency and its harmonics is significantly greater. It is also observed that several of the frequencies with large amplitudes lies in the frequency spectrum below blade passage frequency. Running the simulations on a sector model containing only one of the blades would probably lead to a different result in this spectrum.

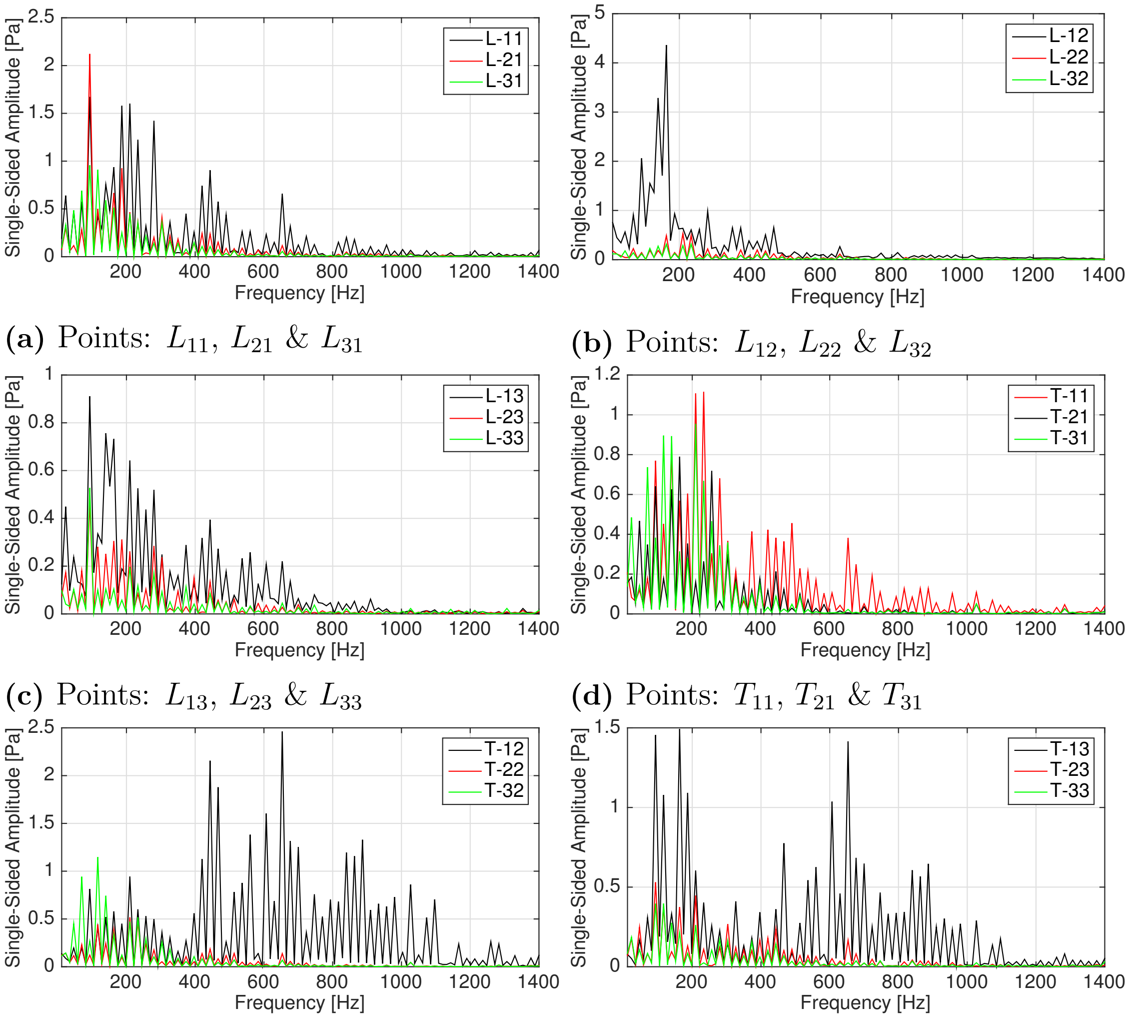

(a) Points: L_{11}, L_{21} & L_{31}

(b) Points: L_{12}, L_{22} & L_{32}

(c) Points: L_{13}, L_{23} & L_{33}

(d) Points: T_{11}, T_{21} & T_{31}

(e) Points: T_{12}, T_{22} & T_{32}

(f) Points: T_{13}, T_{23} & T_{33}

Figure 4.10: Single-sided amplitude spectrum of the static pressure in eighteen points on one of the fan blades. A fast fourier transform algorithm is employed to calculate the spectrum.

4.2.6 Comparison Deformed vs. Undeformed

Static pressure in six of the blade sampling points obtained during simulation 12 and 13 (see Table 3.4) is used to investigate the impact of running the CFD analysis with the original undeformed geometry versus running it with the geometry deformed due to the rotation. The result is presented in Figure 4.11, which is showing the static pressure as a function of rotational angle during one revolution, and in Table 4.4, where the data from the figures is summarised. The time varying pressure exhibit similar behaviour with a differences in fluctuation amplitude of approximately 1 Pa and a difference in average pressure of approximately 10 Pa.

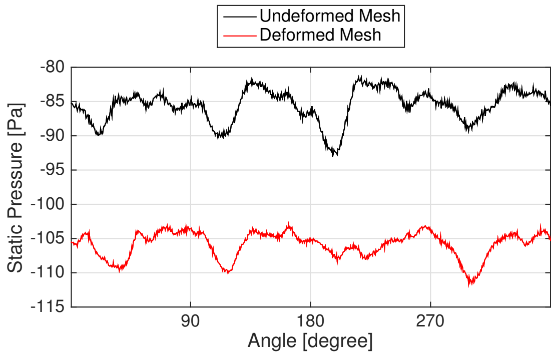

(a) L_{21}

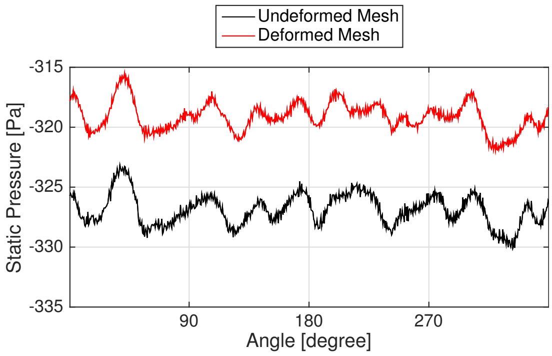

(b) T_{21}

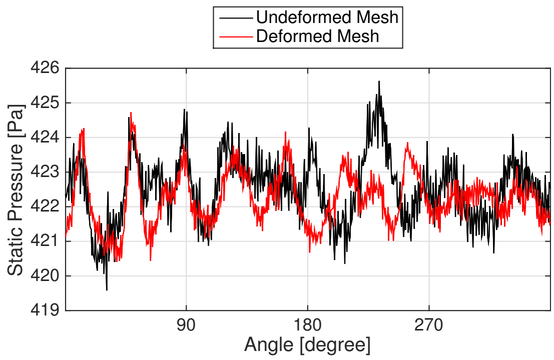

(c) L_{22}

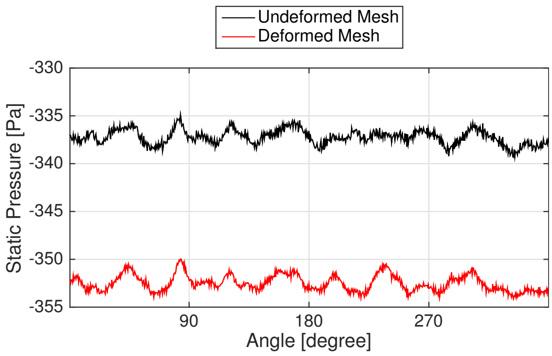

(d) T_{22}

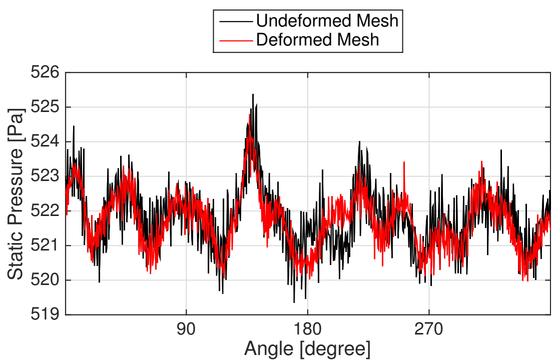

(e) L_{23}

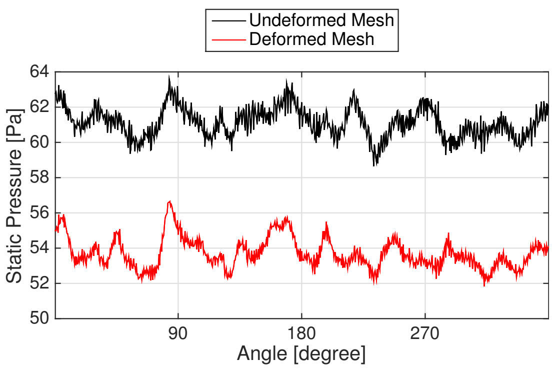

(f) T_{23}

Figure 4.11: Static pressure during the fifth revolution on six different locations as a function of rotational angel

Table 4.4: Static pressure data comparison between the deformed and the undeformed mesh during revolution five.

		Location					
		L_{21}	T_{21}	L_{22}	T_{22}	L_{32}	T_{32}
Undeformed mesh	Amplitude [Pa] (largest cycle)	5,8	3,5	3,0	2,2	3,0	2,5
	Mean [Pa]	-85,0	-326,9	422,5	-337,2	521,8	61,1
Deformed mesh	Amplitude [Pa] (largest cycle)	4,3	3,2	2,2	2,1	2,4	2,4
	Mean [Pa]	-105,9	-319,1	422,2	-352,5	521,7	53,7
Ratio Def/Udef	Amplitude [%] (largest cycle)	74,7	92,2	71,4	93,3	80,0	97,7
	Mean [%]	124,7	97,6	99,9	104,5	100,0	87,9

4.2.7 Inlet Helices

In Figure 4.12 Isohelicity surfaces created with results obtain in simulation 12 (see Table 3.4) are shown. The Isohelicity surfaces are created in the middle-zone and they are visualised from the inlet direction at four subsequent time instances. The fan is rotated ten degrees between each time instant. When comparing the Isosurfaces at the different time instances, it is noted that the fan inlet structures, starting at the nozzle walls and travelling down into the fan, are stationary relative to the fan rotation. The fan rotation can be seen by comparing the location of the black surface in these plots, which represents one of the fan sectors. It is further noted that a correlation can be seen between the inlet helices and the pressure fluctuations on the blades by monitoring the static pressure on one of the blades as it passes the helices. The static pressure on the two pressure points closest to these inlet helices, L_{11} and T_{11}, are plotted in Figure 4.13 and in Figure 4.14. The vertical lines in Figures 4.13 and 4.14 are drawn at locations of local maxima and minima respectively. The time corresponding to respective line is then used to plot the point's (L_{11} and T_{11}) location in respect to the inlet helices in one of the isohelicity surfaces in Figure 4.15. Which can be done since the inlet helices is stationary in space as the fan rotates. It can be noted that a pressure fluctuation occurs when the sampling point passes one of the helices.

(a) 0 °

(b) 10 °

(c) 20 °

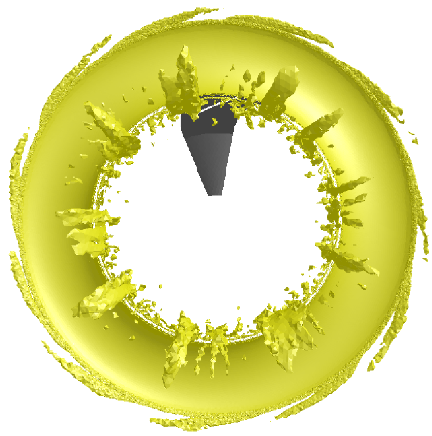

(d) 30 °

Figure 4.12: Isohelicity surface (2000 m/s^2) in the middle-zone visualised from the inlet direction at four subsequent time instances. The fan has rotated 10 degrees between each figure, translating into a time of approximately 1,2 ms.

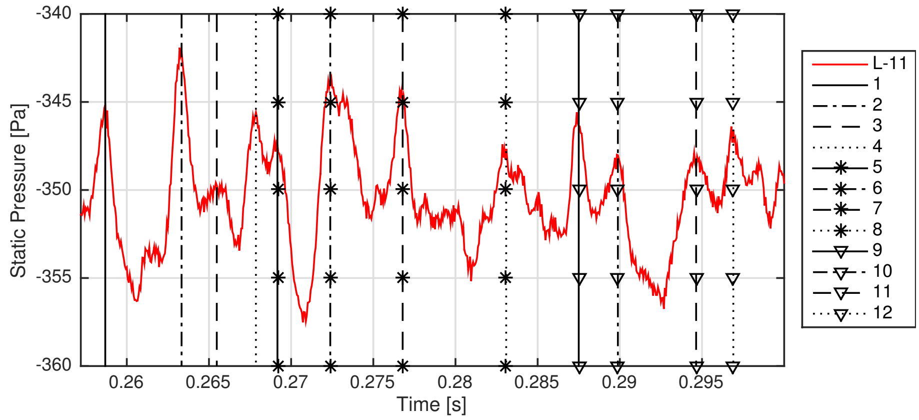

Figure 4.13: Static pressure at point L_{11} during one fan revolution. The vertical lines are plotted at locations of local pressure maxima.

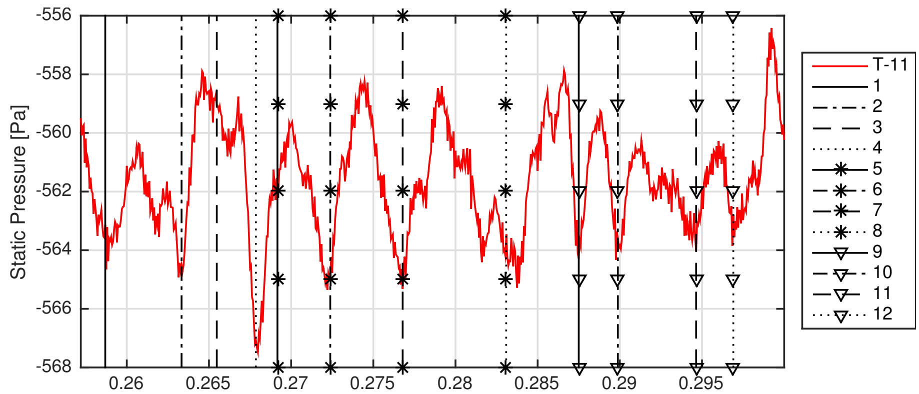

Figure 4.14: Static pressure at point T_{11} during one fan revolution. The vertical lines are plotted at locations of local pressure minima.

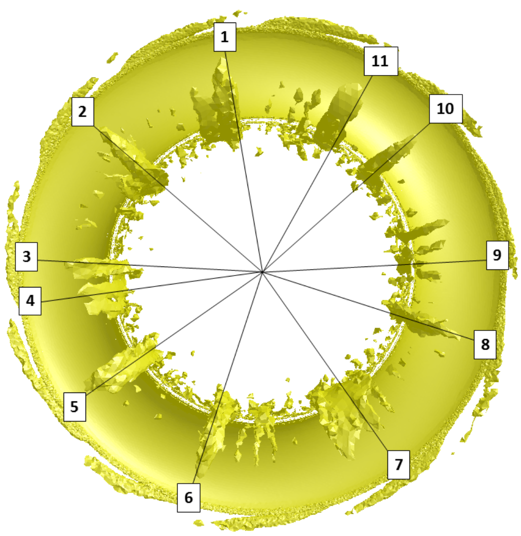

Figure 4.15: Isohelicity surface (2000 m/s^2) in the middle zone visualised from the inlet direction at time $\approx 0,3$ s. The lines are plotted to connect the inlet helices seen in this figure with the local extrema in Figure 4.13 and in Figure 4.14.

5

Discussion

The Discussion is divided in three parts. In the first part the implemented methodology is discussed with focus on weaknesses and possible improvements. The last two parts deals with the results, possible explanations and implications are presented, starting with FEA followed by CFD.

5.1 Methodology Related

The following section treats issues encountered during the project related to the simulation procedures. Noted weaknesses are discussed as well as possible areas of improvements. The frictional contacts implemented in the structural analyses are discussed first, followed by implications related to the cyclic symmetry boundary condition, and the section is ended with a discussion about the implemented verification methods.

The coefficient of friction set for the contacts described in section 3.3.3 was not carefully set with respect to material and operating conditions of the fan. A coefficient of friction close to 1 represents aluminium better than the chosen value of $0,2$ [31]. A friction coefficient over $0,2$ can cause slow convergence which has been observed in static analysis tests on a coarse mesh for the sector model. Setting a value over $0,2$ causes ANSYS to issue a warning message which urges the user to pay extra attention to contact definitions to improve convergence properties. However, increasing the the coefficient to 1 gives a negligible change in maximum deflection and only a variation of ≈ 4 MPa (≈ 2 %) in principal stress in a point like P_3. Therefore, no further investigation was done on the impact of the friction coefficient. Modelling the frictional contact can be a complicated matter in it self and is not included in the scope of this work.

To transfer displacements to the CFD mesh which models the whole fan, structural analysis must also be done on the whole fan in ANSYS workbench. The result of static analysis on the full fan can also be obtained by implementing cyclic symmetry boundary condition on the sector model which is more efficient in terms of computational resources. It would be desirable to treat the result of cyclic symmetry analysis as a whole fan model which would allow for displacements to be transferred to the fluid mesh. No solution was found for this in ANSYS 17.0. Efficiency improvements can be made by looking into this issue when performing the same analysis in a future release of ANSYS or another software.

As mentioned in section 3.3.2, cyclic symmetry was not available in a transient structural analysis in ANSYS Mechanical. Therefore, the displacements on the cyclic boundary were fixed to represent the displacements caused by the centrifugal force. This is deemed a close approximation of the true displacements after the evaluation in Equations 4.1 and 4.2, which shows that the applied aerodynamic forces has little impact on the structure. However, the effect on the dynamics of the structure by fixing the displacements on the cyclic boundary has not been investigated. The possible vibrations in the structure would be induced by the fluctuating part of the pressure which is much smaller than the steady state pressure. Therefore, reasoning can be made that the fluctuating part of the pressure would have a very limited impact on the structure regardless of the fixed boundary condition since it is so small. To capture the dynamic effects, the whole fan should be considered in the transient analysis. If the dynamic effects are significant a two-way FSI analysis must be done to account for the structural displacements in the CFD analysis.

The lack of verification methods is considered to be the primary shortcoming of this project. Although numerical simulations of fluid and solids as well as their interaction have been available for many years, validity of the results is case dependent and should be investigated with great care. Verification would, in the ideal case, have been preformed against transient blade pressure and weld stress measurements obtained in controlled test facilities. One of the reasons for conducting this project was that test facilities with this type of capabilities were not available and numerical simulations were therefore used in its place. Simulation methods verified for similar applications was used when possible to counteract the lack of experimental data.

5.2 FEA Results

The maximum deflection in the full fan model is considered satisfying when compared to maximum deflection achieved in the mesh convergence study. The finest mesh in the mesh convergence study (sector A) consists of 592×10^3 elements which can be compared to the full models 727×10^3 which leads to the conclusion that the mesh for the full model performs well. A notable difference between the mesh in the convergence study and the full model is the element types used. The full model is meshed with some hexahedral elements which keeps the element count down while preserving element size and element quality.

Sector model B that was used when calculating cyclic boundary displacements for the transient FEA also give reasonable result of maximum displacement when compared to the mesh convergence study. The impact of merging the flanges to Back- and Frontplate does not seem to affect the displacement field much. It can be expected that merging the parts instead of using a MPC contact would result in a softer structure since MPC bonds are rigid. Therefore, the slightly lower maximum displacement is probably due to a coarser mesh.

The change in displacements on the cyclic boundary by adding aerodynamic loads are so small (order of 10^{-3} mm) in this context that the assumption of neglected them in the transient FEA is deemed reasonable as long as the fan's eigenfrequencies are not excited. When eigenfrequencies are exited the problem of dynamic stability arise which is not investigated in this work. Since impact of aerodynamic loads are so small at the cyclic boundary it is reasonable to assume that the stress near the welds are not significantly affected by fixing the cyclic boundary displacements.

Since the pressure was sampled from the deformed CFD mesh and mapped onto the undeformed structural model, the source points did not lay perfectly on the geometry surfaces when mapped onto the structural model. This is apparent on the leading edge where the maximum deflection is located. Since the deformations are relatively small and the mapping was partitioned so that surfaces were mapped individually to prevent source points being mapped to any surface other than the corresponding source surface, the accuracy is considered sufficient. However, if deformations would be significantly larger, action might need to be taken to map the pressure on the deformed structural model.

The highest stress range in the stress histories is found at point P_3 because of a relatively low stress at the first time step, shown in Figure 4.7c. Since the first and second time-step were loaded identically to avoid dynamic effect of sudden load application, the increase between first and second time-step is probably due to better convergence value at the second time-step. Accounting for this, the stress range for P_3 is considerably lower and the largest stress range is then found at P_1, at ≈ 0.1 MPa (Figure 4.7a) instead. The stress often exceeds the yield limit for the material at stress concentrations near the flanges and welds. To get a more realistic stress values a more complex material model should be implemented. Also critical areas need to be modelled more carefully, like the weld joints. The assumption of linear elastic material is deemed sufficient for this study as the stress range is of interest and not the absolute stress values.

The stress variations presented for points $P_1 - P_4$ follow the same pattern as for the pressure fluctuations; higher frequency close to the trailing edge and larger stress range close to the leading edge. When making the crude estimate of fatigue resistance according to [20], the evaluation should be based on the nominal stress of the component which is being evaluated. In this evaluation the highest stress range found close to a weld is used in order to be conservative. At the low stress ranges calculated in this work, there is little reliability in the exact number of cycles calculated. However, it is clear that, under all assumptions made in this work, there is no risk of fatigue due to the aerodynamic loads. Assumption of infinite life is often made for these stress ranges. Reasoning can be made that the damage caused by accelerating the fan to operating speed and bringing it down to a halt again, creating a load cycle, is much more severe than damage caused by pressure fluctuations. Therefore, the pressure fluctuations can be neglected in fatigue estimation.

5.3 CFD Results

The current section contains discussion about some of the results obtained during the fluid simulations. Possible reasons for why certain results are obtained as well as what implications they bring are treated. The results discussed are: the PQ-curve, transfer of displacements to the fluid domain and pressure fluctuations.

The PQ-curve obtained trough simulations shows a similar trend as the experimentally determined PQ-curve but with a overestimate of pressure increase for all flow rates, shown in Figure 4.8 and in Table 4.1. Several possible reasons have been noted. The model geometry used in the simulations have several differences compared to the geometry used in the test facility. Simplifications of the geometry have been made to ease the mesh generation and computational costs, details of the simplifications can be found in section 3.2. One such simplification that is likely to have an impact on the pressure increase is that the gaps between the blade and the Front- and Backplate have been filled in the fluid domain model, shown in Figure 3.9. In these gaps, air from the leading (pressure) side can travel to the trailing (suction) side, resulting in losses. It should also be noted that the geometric tolerances included in the fan manufacturing process are relatively large resulting in each fan being unique and more or less consistent with the geometry used to create the fluid domain. Another possible explanation is the chosen numerical procedure. The calculated values in the PQ-curve were obtained through steady state simulations using a moving reference frame. This method forces the otherwise inherently unsteady flow in the fan to a steady state solution where the rotation is simulated through source terms and not actual rotation of the fan, described in section 2.5.5. Belonging to the numerical procedure is also the choice to solve the averaged naiver stokes equations which results in the use of turbulence models that are more or less able to represent the turbulent flow structures.

The impact of running the fluid simulations on a geometry deformed under centrifugal loads compared to undeformed geometry is noticeable. Differences in both pressure fluctuation amplitude and mean are apparent, as visible in Figure 4.11 and Table 4.4. It can be concluded that deformation due to centrifugal loads should be considered if accurate estimations of the blade pressure is sought for. Although using the deformed mesh to obtain the fluid loads would not have been necessary in the current case as the fluid loads are to small to have an impact in the life estimates. These results can also be used when evaluation the choice of one-way coupling for the transient calculations. The blade deformation due to rotational loads is as largest around 1 mm, shown in Figure 4.1, which have a impact of the pressure in the studied points that is less than 20 Pa. Deformation due to fluid loads is as largest around $0,01$ mm, which is a result of a pressure difference between the blade sides of several hundred Pa. Hence, one can draw the conclusion that one-way coupling between the fluid and structure for a fixed rotational speed is sufficient, since the fluid loads have little to non possibility to impact the blade deformation to such an extent that the blade pressure will be effected by the new deformed shape.

Limited research was found related to blade pressure fluctuations on centrifugal fans. One report studying pressure fluctuations on a similar centrifugal fan was found [2]. A conclusion made in [2] is that the pressure fluctuations on the blade mainly is a consequence of the blade cutting trough a quasi stationary helical inlet vortex. A somewhat related but different result was found in the process of trying to replicate this inlet vortex. Several inlet helices correlated to the largest pressure fluctuation was observed, these results are presented in section 4.2.7. Potential causes for the creation of these have not been examined further, but it is proposed as a future research topic. More insight into the origin of these inlet helices and how their size can be controlled, could potentially lead to the knowledge of how to design fans that experience less blade pressure fluctuations. In the same report it is also observed that simulations can be implemented to accurately estimate the frequencies of the blade pressure fluctuations but not to accurately estimate their amplitudes. Similar results have been found in another report studying pressure fluctuations in centrifugal fans [32]. Therefore, it is left as a recommendation that results should be verified with test results if accurate pressure fluctuation amplitudes is sought for. It is also advised to model the whole fan and thereby not making use of its cyclic symmetry when simulating the fluid domain. This is a consequence of the correlation between inlet helices and pressure fluctuations. The inlet helices are not cyclic symmetric which potentially would result in a different blade pressure result if only one sector would be modelled. The same conclusion can also be drawn by examining the results in section 4.2.5, where it is noted that the blade pressure frequency spectrum contain significant amplitudes for frequencies below blade passage frequency.

6
Conclusion

This study set out to answer the question of whether fatigue analysis of centrifugal fans can be improved by incorporating fluid-structure interactions. Additionally a numerical method for performing fluid-structure interactions on centrifugal fans are sought for. The current method for evaluating fatigue only incorporates centrifugal loads due to the inertia of the fan, but it is proposed that pressure loads exerted by the fluid on the structure has impact on the life of the fan.

The procedure used for evaluating the fan is solely numerical and performed with the ANSYS Workbench platform. The fluid field is simulated in ANSYS Fluent and the structural field in ANSYS Mechanical. The interaction between the fields is treated through a specially adopted one-way coupling method, in which the transfer between the fields is exclusively from fluid to structure, with one exception: Displacements of the structure resulting from the centrifugal loads is transferred to the fluid domain.

This study has concluded that the fluid structure interactions have insignificant impact on the fatigue life of the studied fan. Stress range due to fluid-structure interactions in the area most prone to fatigue is roughly 0,1 MPa. This stress range translates to approximately 0,2 % of the lowest value included in the S-N curve for aluminium used when estimating fatigue limit in the design codes for welds [20]. The fan stiffness is large in comparison to fluid loads, resulting in small structural deformations and weak coupling between the fields, making one-way FSI a adequately accurate method. The developed FSI method is considered as easily implemented and relatively computationally inexpensive in compassion to other alternatives available in ANSYS Workbench.

The main weakness of this study is the lack of data available to verify the results. In the process of modelling and simulating, a number of more or less valid simplifications had to be made, potentially altering the results. A means of validation is hence considered as future work. Validation would ideally be made through comparisons of numerical results and measurements obtained in a controlled test facility. Pressure fluctuations on the blade and stresses in the welds would be of special interest to validate. The stress amplitude due to fluid-structure interactions obtained trough tests may be considerably higher than what was found in simulations. However, since a drastic increase in stress amplitude is required to influence the fatigue limit, it is likely that exclusion of fluid loads in the fatigue analysis will not effect the estimated life considerably nevertheless.

Bibliography

[1] Donald E. Thompson Jong-Soo Choi Dennis K. McLaughlin. Experiments on the unsteady flow field and noise generation in a centrifugal pump impeller. *Journal of Sound and Vibration* **263 (2003)** (2002), 493–514.

[2] T. H. Carolus D. Wolfram. Experimental and numerical investigation of the unsteady flow field and tone generation in an isolated centrifugal fan impeller. *Journal of Sound and Vibration* **329** (2010), 4380–4397.

[3] J. N. Reddy. *An introduction to Continuum Mechanics.* Cambridge University Press, New York, 2008.

[4] Inc ANSYS®. *ANSYS® Mechaincal APDL Theory Reference.* Vol. 17.1. Southpointe, 2600 ANSYS® Drive, Canonsburg, PA 15317, 2016.

[5] M. Ekh. *Mechanics of solids & fluids. Part I: Fundamentals.* Tech. rep. Div. of Material and Computational Mechanics, Chalmers University of Technology, Göteborg, Sweden, 2016.

[6] Peter Wriggers. *Computational Contact Mechanics.* Second Edition. Springer, 2006.

[7] S. B. Pope. *Turbulent Flow.* Cambridge University Press, Cambridge, UK, 2001.

[8] L. Davidson. *Fluid mechanics, turbulent flow and turbulence modeling.* Tech. rep. Div. of Material and Computational Mechanics, Chalmers University of Technology, Göteborg, Sweden, 2017.

[9] B. E. Launder and D. B. Spalding. *Lectures in Mathematical Models of Turbulence.* Academic Press, London, 1972.

[10] D. C. Wilcox. *Turbulence Modeling for CFD.* DCW Industries, Inc. La Canada, California, 1998.

[11] M. Kuntz F. R. Menter and R. Langtry. "Ten years of industrial experience of the SST turbulence model". K. Hanjalić, Y. Nagano, M. J. Tummers (Editors), Turbulence Heat, and Mass Transfer 4, pages 624-632, New York, Wallingford (UK), 2003. begell house, inc.

[12] F. R. Menter. Influence of freestream values of $k - \omega$ turbulence model predictions. *AIAA Journal* **30** (6 1992), 1657–1659.

[13] Inc ANSYS®. *ANSYS® Fluent Theory Guide.* Southpointe, 2600 ANSYS® Drive, Canonsburg, PA 15317, 2016.

[14] Frank M. White. *Fluid Mechanics.* 7th ed. McGraw-Hill Companies, Inc. 1221 Avenue of the Americas, New York, NY 10020, 2011.

[15] W. Malalasekera H. Versteeg. *An Introduction to Computational Fluid Dynamics: The Finite Volume Method.* Second Edition. Pearson Education Limited, 2007.

[16] *See the MRF Development*. 2009. URL: `https://openfoamwiki.net/index.php/See_the_MRF_development`.

[17] A. Dervieux. *Fluid-Structure Interaction*. Innovative Technology Series. ISTE Publishing Company, 2003.

[18] F. Inada M. Kato K. Ishihara T. Nishihara N. Mureithi M. Langthjem T. Nakamura S. Kaneko. *Flow-Induced Vibrations*. Second Edition. Elsevier Ltd., 2013.

[19] J. P. Hurtado-Cruz C. Santolaria-Morros Sandra Velarde-Suárez R. Ballesteros-Tajadura. Experimental determination of the tonal noise sources in a centrifugal fan. *Journal of Sound and Vibration* **295** (2006).

[20] A.F Hobbacher. *Recommendations for Fatigue Design of Welded Joints and Components*. 2nd ed. Springer International Publishing Switzerland 2016, 2014.

[21] G. Delibra A. Corsini and A. G. Sheard. A Critical Review of Computational Methods and Their Application in Industrial Fan Design. *ISRN Mechanical Engineering* **2013** (2013).

[22] Inc ANSYS®. *ANSYS® Meshing User's Guide*. Vol. 17.1. Southpointe, 2600 ANSYS® Drive, Canonsburg, PA 15317, 2017.

[23] E. Sjösvärd. "Numerical Estimation of the Aerodynamic Tones Radiated From a Centrifugal Fan". MA thesis. Chalmers University of Technology, 2016.

[24] Inc ANSYS®. *ANSYS® Fluent User's Guide*. Vol. 18.0. Southpointe, 2600 ANSYS® Drive, Canonsburg, PA 15317, 2017.

[25] Inc ANSYS®. *ANSYS® System Coupling User's Guide*. Vol. 17.1. Southpointe, 2600 ANSYS® Drive, Canonsburg, PA 15317, 2017.

[26] P.G. Huang J. E. Bardina and T. J. Coakley. Turbulence modeling, validation, testing and development. *NASA Technical Memorandum* **110446** (1997).

[27] S. Kouidri M. Younsi F. Bakir and R. Rey. Numerical and experimental study of unsteady flow in a centrifugal fan. *Proceedings of the Institution of Mechanical Engineers, Part A: Journal of Power and Energy* **221** (2007).

[28] *ANSYS®, Inc Modeling Rotating Machinery with ANSYS Fluent*. Link to site. Accessed: 2017-05-24. Note that an Ansys customer portal account is needed to access this material.

[29] C. Xu and Y. Mao. Passive control of centrifugal fan noise by employing open-cell metal foam. *Applied Acoustics* **103** (2016).

[30] J. P. Hurtado-Cruz R. Ballesteros-Tajadura S. Velarde-Suárez and C. Santolaria-Morros. Numerical Calculation of Pressure Fluctuations in the Volute of a Centrifugal Fan. *Journal of Fluids Engineering* **128** (2006).

[31] *Coefficient of Friction Equation and Table Chart*. 2017. URL: `http://www.engineersedge.com/coeffients_of_friction.htm`.

[32] S. Kouidri M. Younsi F. Bakir and R. Rey. Influence of Impeller Geometry on the Unsteady Flow in a Centrifugal Fan: Numerical and Experimental Analyses. *International Journal of Rotating Machinery* **2007** (2007).

A

Appendix 1

A.1 Python Script

This short python script is implemented in the external data modules shown in Figure A.2 to rotate the source nodes from the CFD analysis to the coordinate system of the FE model.

```python
# encoding: utf-8
# Release 17.0
SetScriptVersion(Version="17.0.323")
system1 = GetSystem(Name="SYS 9") #Get variables from desired external data module
setup1 = system1.GetContainer(ComponentName="Setup")
externalLoadData1 = setup1.GetExternalLoadData()
string="ExternalLoadFileData"
rotation=-2256  #Rotation from initial position of last time step

#For-loop to rotate the coordinates for all time steps
for i in range(0,180):
 if i==0:
        n=""
 else:
        n=" "+str(i)
  externalLoadFileData1 = externalLoadData1.GetExternalLoadFileData(Name=string+n)
  externalLoadFileDataProperty1 = externalLoadFileData1.GetDataProperty()
  rotation=rotation-2
  externalLoadFileDataProperty1.ThetaXY = 0
  externalLoadFileDataProperty1.ThetaXYUnit = "degree"
  externalLoadFileDataProperty1.ThetaXY = rotation
```

A.2 Workbench Connections

The connections made in Workbench to transfer data between analyses are shown in Figure A.1 and A.2.

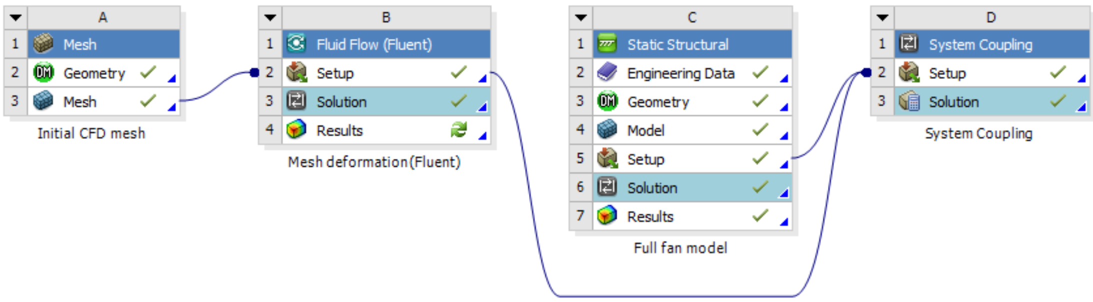

Figure A.1: Workbench setup of transferring displacements from the full fan model to the CFD mesh and deforming it in Fluent

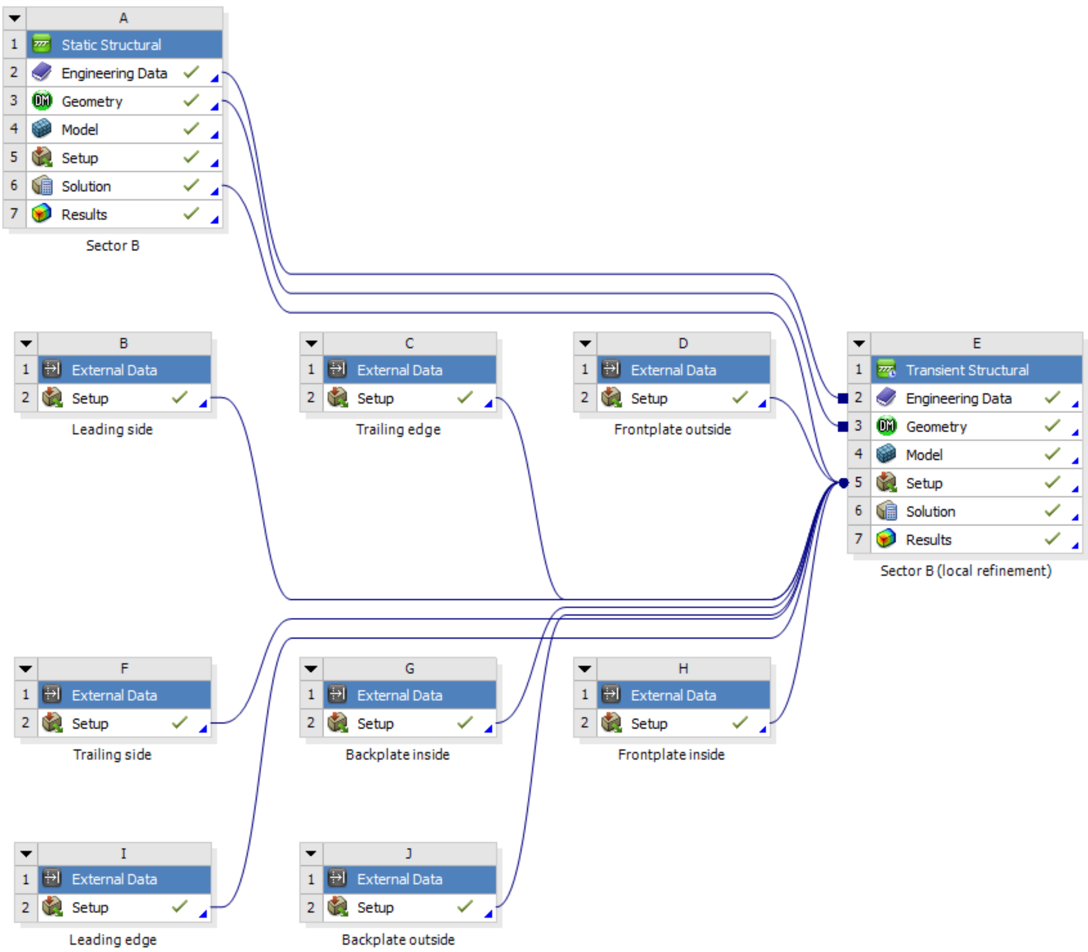

Figure A.2: Workbench setup of the transient FE analysis. Each external data module contains pressure data from different surfaces of the fan which are imported to the transient FE analysis. Static structural analysis transfers boundary displacements to the transient analysis